Refining spectroscopic calculations for trivalent lanthanide ions: A revised parametric Hamiltonian and open-source solution

Juan-David Lizarazo-Ferro [1,*] Tharnier O. Puel [2,*] Michael E. Flatté [2,3,†] and Rashid Zia [1,‡]

[1]*School of Engineering and Department of Physics, Brown University, Providence, Rhode Island 02912, USA*

[2]*Department of Physics and Astronomy, University of Iowa, Iowa City, Iowa 52242, USA*

[3]*Department of Applied Physics and Science Education, Eindhoven University of Technology, Eindhoven, Netherlands*

(Received 9 April 2025; revised 27 September 2025; accepted 9 December 2025; published 13 February 2026)

The historical calculation of spectroscopic properties for trivalent lanthanide ions is a complex multistep process that has been prone to inaccuracies. In this work, we revise the parametric semi-empirical Hamiltonian and address long-standing discrepancies in the literature. We also resurface the distinctions between orthogonal and non-orthogonal operators, and use orthogonalized operators to provide an alternative parametric description. Based on experimental data available in the literature, an updated set of parameter values for the canonical case of lanthanide ions in LaF_3 is presented. Additionally, we provide calculations of spontaneous emission rates and oscillator strengths for magnetic dipole transitions in the LaF_3 crystal host. To ensure the replicability of our findings, we make available the open-source code `qlanth`, accompanied by a comprehensive set of electronic files to serve as an updated reference for future calculations.

DOI: 10.1103/llzb-wrlg

I. INTRODUCTION

Trivalent lanthanide ions (Ln^{3+}) are interesting because of their narrow optical transitions, which arise from the shielding of their $4f$ electrons by the outer $5s^2$ and $5p^6$ closed shells [1–3]. Having unpaired $4f$ electrons, the Ln^{3+} ions constitute spin defects useful for lasers and amplifiers [4,5], magnetic resonance imaging [6], and quantum technology [7–10]. Furthermore, the distinctive intra-$4f$ transitions are appealing for exploring fundamental topics in atomic [11] and optical [12–14] physics.

The trivalent lanthanides are often theoretically described by a Hamiltonian with adjustable parameters that are fitted empirically to experimental data. Using this description, one obtains an approximate electronic structure, including eigenstates, from which one may calculate optical transition rates and oscillator strengths for magnetic dipole transitions [15], forced electric dipole transitions through Judd-Ofelt theory [16,17], as well as g-tensors for ground-state excitations [18,19]. Shielding of the $4f$ shell simplifies the study of a lanthanide ion across different hosts, and within the same host, systematic studies across the lanthanide row reveal that many model parameters follow relatively simple trends [20–22]. The canonical example of such systematic studies is the work by Carnall *et al.* [21], which has been widely cited and continues to be used to various degrees of depth. In the simplest usage, the energy spectra for the original lanthanum trifluoride (LaF_3) crystal host are simply referenced to identify observed transitions [23]. In a more elaborate usage, the parameters for LaF_3 may be used as starting values for fitting the data for different crystal hosts [24,25]. Furthermore, the eigenvectors can be used to calculate the magnetic susceptibility as a function of temperature [26,27]. The canonical work of Carnall *et al.* is often taken as a theoretical starting point for the inclusion of additional terms to the semi-empirical Hamiltonian such as correlation crystal field [28,29], hyperfine interaction [30], spin-correlated crystal field [31], and exchange interactions [32].

However, this canonical approach has some shortcomings. Calculations with the semi-empirical Hamiltonian are complex, and this complexity makes it prone to inaccuracies [33,34]. The calculations generally rely on the application of the methods developed by Racah [35–38] combined with precalculated spectroscopic tables that have been found to contain multiple errors [33,39,40]. Furthermore, the calculations are somewhat ambiguous, because there are several possible ways to parametrize the relevant interactions [20,41].

Even after errors were recognized, the parameters provided by Carnall *et al.* [21] more than three decades ago have been used repeatedly and without update. For example, just recently, they have been used to estimate crystal field parameters for Dy^{3+} in rare-earth oxides [42], hyperfine interactions for Ho^{3+} in yttrium orthosilicate [30], dipolar interactions between Gd^{3+} in rare-earth oxides [43], and the g-tensor for Er^{3+} implanted into silica [44]. Furthermore, errors in the original calculation may be obscured when fitting the model parameters, yielding similar closeness to the experimental energies, at the cost of inaccuracy in the eigenvectors.

This paper revisits the canonical work of Carnall *et al.* [21]. The relevant spectroscopic tables for the semi-empirical Hamiltonian are recalculated, addressing both previously noted errors as well as newly identified ones. Then, by detailed analysis of the magnetic contributions in the calculated spectra, we present and correct for incongruencies in the claimed inclusion by Carnall *et al.* of the spin-spin interaction.

*These authors contributed equally to this work.

†Contact author: michaelflatte@quantumsci.net

‡Contact author: rashid_zia@brown.edu

Furthermore, an ongoing challenge in physics is the difficulty of reproducing published research [45]. Besides some theoretical challenges, the semi-empirical approach suffers from practical challenges, many of which we aim to resolve here. Currently available computer codes for doing these calculations are not only outdated, but they yield incompatible results (i.e., the same set of parameters leads to distinct spectra), and their internal calculations are not sufficiently documented. Here, we present a modern, well-documented, publicly available implementation written in *Wolfram* language, called `qlanth` [46], offering solutions to many of these deficiencies.

In Sec. II, we introduce the Hamiltonian and its mapping to the parametric semi-empirical Hamiltonian within the single-configuration approximation. In Sec. III, we compare our calculations to the literature, as well as to other code implementations. Sections IV and V offer updated fitted parameters—together with a collection of reproducible data including energies, eigenvectors, and optical transitions—that provide an updated reference for the spectroscopy of trivalent lanthanide ions.

II. PARAMETRIC SEMI-EMPIRICAL HAMILTONIAN FOR THE $4f$ ELECTRONS IN THE SINGLE-CONFIGURATION DESCRIPTION

A fundamental description of the electromagnetic interactions for the f electrons of lanthanide ions embedded in a crystal host may be represented by the following Hamiltonian:

$$\begin{aligned}\mathcal{H} = {} & \mathcal{H}_{\mathrm{K}} + \mathcal{H}_{\mathrm{n}} + \mathcal{H}_{e\text{-}e} + \mathcal{H}_{\mathrm{s\text{-}o}} \\ & + \mathcal{H}_{\mathrm{s\text{-}s}} + \mathcal{H}_{\mathrm{o\text{-}o}} + \mathcal{H}_{\mathrm{s\text{-}o\text{-}o}} + \mathcal{H}_{\mathrm{CF}}. \end{aligned} \tag{1}$$

The main contributions are the kinetic (K), nuclear (n), Coulomb (e-e), and spin-orbit (s-o) terms. Besides the main contributions, there are additional magnetic interactions beyond the single-electron spin-orbit ($\boldsymbol{s}_i \cdot \boldsymbol{l}_i$) term that need to be considered to take into account relativistic corrections that are not negligible in heavier atoms. These relativistic contributions may be derived from the Breit Hamiltonian resulting in two-body interactions including spin-spin ($\boldsymbol{s}_i \cdot \boldsymbol{s}_j$), spin-other-orbit ($\boldsymbol{s}_i \cdot \boldsymbol{l}_j$) [2,47–52], and orbit-orbit ($\boldsymbol{l}_i \cdot \boldsymbol{l}_j$) [2,49,52–54]. Finally, the influence of the host is included as an effective potential (CF) with the appropriate symmetry for the crystal host.

An approximate solution to the Hamiltonian in Eq. (1) can be obtained by limiting the Hilbert space to the $4f^N$ ground configuration, where N is the number of electrons in the $4f$ shell. The single (ground) configuration $4f^N$ opposes a more generic approach that includes the occupation of additional (excited) orbitals in the Hilbert space, discussed later in the configuration-interaction treatment. In the single-configuration description, a particular basis state is labeled by specifying its S, L, J, and M_J quantum numbers, and is usually written as $|\psi\rangle = |f^N \tau SLJM_J\rangle$ state, where τ is an additional quantum number that accounts for the degeneracy of the LS terms. The matrix elements are analyzed using the algebra of irreducible tensor operators developed by Racah [35–38], in which the angular part can be calculated explicitly, and the radial part subsumed as multiplicative coefficients. More precisely, matrix elements of the form $\langle\psi_i|\mathcal{H}|\psi_j\rangle$ need to be determined, where i, j run over all the states $|f^N \tau SLJM_J\rangle$. Racah algebra allows computing each matrix element in the form $p\langle\psi_i|\hat{\mathcal{O}}|\psi_j\rangle$, where the operator $\hat{\mathcal{O}}$ contains the angular part and the radial part p is a coefficient later treated as a fitting parameter. Once these reduced matrix elements have been determined for the configurations f^N with $N \leqslant 3$, then the method of fractional parentage [38] is used to determine them for f^{N+1}. Further details of the calculations of such matrix elements are well documented in Refs. [2,55] and will not be repeated here. In the following, however, we will summarize how the form of Hamiltonian shown in Eq. (1) is transformed to the form actually used in calculations as given ahead in Eq. (2). A summary of this mapping is given in Appendix A.

First, the kinetic energy and nuclear potential energy ($\mathcal{H}_K$ and $\mathcal{H}_n$) depend only on the number of electrons N, are constant over the states of the ground configuration, and are noted as $\mathcal{H}_0 + \epsilon$ in Eq. (2), where ϵ is a constant shift used to optimize the fitting, following common practice [21,24]. Second, the next largest contribution to the energy spectrum comes from the Coulomb term ($\mathcal{H}_{e\text{-}e}$). The calculation of the matrix elements involving the Coulomb term leads to the set of parameters $F^{(k)}$ and operators $\hat{f}_k$, where k corresponds to the order of the Slater radial integral, and where only $k = 0, 2, 4, 6$ need to be considered as per selection rules of integrals of products of three spherical harmonics. Third, a large contribution also comes from the spin-orbit term ($\mathcal{H}_{\mathrm{s\text{-}o}}$), which reduces to a single fitting parameter ζ and the operator $\hat{s}_i \cdot \hat{l}_i$ for the ith electron.

As a result, the parametric semi-empirical Hamiltonian can be written as [2]

$$\begin{aligned}\mathcal{H}_{\mathrm{para}} = {} & (\mathcal{H}_0 + \epsilon) + \sum_{k=0,2,4,6} F^{(k)} \hat{f}_k + \zeta \sum_{i=1}^{N} (\hat{s}_i \cdot \hat{l}_i) \\ & + \alpha \hat{L}^2 + \beta\, \hat{C}(\mathcal{G}_2) + \gamma\, \hat{C}(\mathcal{SO}(7)) + \sum_{k=2,3,4,6,7,8} T^{(k)} \hat{t}_k \\ & + \sum_{k=2,4,6} P^{(k)} \hat{p}_k + \sum_{k=0,2,4} M^{(k)} \left(\hat{m}_k^{\mathrm{s\text{-}o\text{-}o}} + \hat{m}_k^{\mathrm{s\text{-}s}}\right) \\ & + \sum_{i=1}^{N} \sum_{k=2,4,6} \sum_{q=-k}^{k} \mathcal{B}_q^{(k)} \hat{C}_q^{(k)}(i), \end{aligned} \tag{2}$$

where $\hat{L}$ is the total angular momentum of all $4f^N$ electrons, $\hat{C}(\mathcal{G}_2)$ and $\hat{C}(\mathcal{SO}(7))$ are the Casimir operators of groups $\mathcal{G}_2$ and $\mathcal{SO}(7)$, respectively. $\hat{C}_q^{(k)}$ are spherical harmonics with the Racah normalization convention. On first approximation, many parameters in the semi-empirical Hamiltonian have simple integral expressions in terms of the radial part of the single-electron orbitals. However, these expressions become significantly more complex when configuration interaction is included, and estimating the single-electron orbitals is itself a nontrivial task. The semi-empirical approach addresses these theoretical challenges by directly referencing experimental data to determine the value of the model's parameters.

A. Configuration, magnetic, and crystal field interactions

The single-configuration approximation can be much improved by the inclusion of effective terms originating from

configurations other than $4f^N$. These effects constitute the next most important correction to the Hamiltonian and may be calculated using perturbation theory without increasing the size of the Hilbert space. For example, the configuration interaction analysis relevant to the ground configuration $4f^3$ of Nd^{3+} considers configurations like $4f^26s$, $4f^25d$, and $4f^16s^2$. Luckily, for the trivalent lanthanides, the center of the energy spectrum of the $4f$ configuration is well isolated ($\sim 10^4$ cm^{-1}) from other configurations [56], thus interacting only via high energies. This justifies treating the interacting configurations as perturbations to the single-configuration description, which to second order adds terms like $\langle\psi|G|m\rangle\langle m|G|\psi'\rangle/\Delta E_m$ to the Hamiltonian [57], where $|m\rangle$ represents a configuration other than $4f$ and G the Coulomb operator. These perturbations are responsible for the parameters α, β, and γ in Eq. (2), as well as a screening of the $F^{(k)}$ parameters. Moreover, still within second-order perturbation theory, the case of one-electron excitation either from or into the $4f^N$ shell (e.g., $4f^25d$ in Nd^{3+}) needs an additional set of parameters $T^{(k)}$, in which the orbital part involves coordinates of three electrons and thus represents an effective three-body interaction [57,58]. In some hosts where the charge transfer bands are close to the excited states of the $4f^N$ configuration, it is necessary to explicitly consider a hybridization with the ligand wave functions [59,60]. Terms of third order from perturbation theory lead to additional parameters $T^{(11)}, \ldots, T^{(19)}$ with accompanying three-body operators [41,57], which will be disregarded here following common practice.

The configuration interaction analysis can yield additional terms in which different operators are correlated to one another. In addition to the previously discussed contributions, second-order perturbation theory brings extra terms, like $\langle\psi|\Lambda|m\rangle\langle m|G|\psi'\rangle/\Delta E_m$, where Λ is the spin-orbit operator; see Refs. [40,61]. That term is called electrostatically correlated spin-orbit interaction, because of its mixing of G and Λ. In Racah formulation, this term contributes similarly to the spin-other-orbit discussed below, but also requires a set of independent parameters $P^{(k)}$ called the pseudomagnetic parameters.

The magnetic dipolar interaction ($\mathcal{H}_{\text{s-s}}$) contributes with the parameters $M^{(k)}$, which have a radial integral form as defined by Marvin [62], and appears with the $\hat{m}_k^{\text{s-s}}$ operators in the Hamiltonian. The effects of the spin-spin contribution in the energy spectrum (on Pr, Nd, Er in $LaCl_3$) are discussed in Ref. [63]. The next magnetic interaction, the spin-other-orbit ($\mathcal{H}_{\text{s-o-o}}$), contributes in two manners. First, it contributes to modifying the spin-orbit parameter ζ. Second, it also requires $M^{(k)}$ as fitting parameters. Although sharing the same fitting parameters, we explicitly write the operator $\hat{m}_k^{\text{s-o-o}}$ for the spin-other-orbit in Eq. (2) to distinguish it from the dipolar interaction. The reason for that will become clear in the next section, where we make a quantitative comparison with literature results. The orbit-orbit interaction ($\mathcal{H}_{\text{o-o}}$) contributes similarly as α, β, and γ and therefore is parametrically absorbed in the fitting.

Finally, the effect of the crystal field (V_{CF}) from the host material on the $4f$ electrons of the lanthanide ions is taken into account with the $\mathcal{B}_q^{(k)}$ parameters. The nonzero crystal field parameters are determined by the point symmetry of the location of the ions inside of the host crystal, where less symmetry requires more parameters (see discussion in Ref. [23]). The calligraphic $\mathcal{B}_q^{(k)}$ carries both the real and imaginary coefficients, such that $\mathcal{B}_q^{(k)} = B_q^{(k)} + iS_q^{(k)}$.

TABLE I. Maximum splittings between consecutive energies (middle column) and total extent of the spectrum (right column) from the parametrized Hamiltonian. The ranges account for the splittings encountered across all trivalent lanthanides doped into LaF_3. Notice that these ranges are only approximate for the reasons discussed in the main text.

Parameter	Subsequent splitting (cm^{-1})	Total extent (cm^{-1})
$F^{(k)}$	(20000 − 40000)	(45000 − 190000)
ζ	(2000 − 10000)	(2000 − 40000)
α, β, γ	(300 − 1200)	(2000 − 6000)
$T^{(k)}$	(100 − 2000)	(800 − 8000)
$P^{(k)}$	(20 − 200)	(100 − 900)
$M^{(k)}$	(10 − 40)	(100 − 500)
$B_q^{(k)}$	(40 − 500)	(600 − 3000)

B. Parametric semi-empirical Hamiltonian

To build intuition about the relative contribution of each interaction term in Eq. (2) for the case of lanthanide ions in LaF_3, we looked at the maximum energy splitting between subsequent energies, generated by each term individually. This only approximates the contribution of each interaction, because the operators included in the Hamiltonian do not commute. Additionally, their physical origins are not unequivocal, because the same parameter may be enhanced or suppressed by contributions from different physical mechanisms, as discussed in Appendix A. For simplicity, each term will be referred approximately according to its main effect. All things considered, the Coulomb interaction between f electrons ($F^{(k)}$) leads to splittings of the order of 10^4 cm^{-1} and spin-orbit (ζ) is typically 10^3 cm^{-1}. Configuration interaction (α, β, and γ) adds energy splittings of the order of 10^2 cm^{-1}. The three-body terms can be very different among the ions, varying splittings within (10^2–10^3) cm^{-1} from 3 to 12 electrons. Also, the electrostatically correlated spin-orbit interaction ($P^{(k)}$) have smaller contributions of $\sim 10^2$ cm^{-1}. Magnetic contributions ($M^{(k)}$) are even smaller at about 10 cm^{-1}. Finally, the crystal field contribution is of the order of 10^2 cm^{-1}. Table I presents the range of values found across the lanthanide ions in LaF_3.

C. Orthogonal and non-orthogonal operators

Orthogonal operators reduce parameter correlations in Hamiltonian fitting, as originally discussed by Judd, Crosswhite, and Suskin [20,41], even though both orthogonal and non-orthogonal forms yield the same energy spectra when the corresponding coefficients are properly mapped (see Appendix B). While the use of orthogonal operators often results in better fitting precision, as evidenced by smaller residuals in 7 out of 12 cases compared to the non-orthogonal approach (Table VI), they can also lead to larger parameter uncertainties. Note that a fully orthogonal Hamiltonian would require

TABLE II. Additional errors in the *fncross* tables identified here. The row for $n = 7$ was incorrectly attributed to $\langle {}^2\mathrm{F3}|\hat{t}_3|{}^2\mathrm{F8}\rangle$ by Judd and Lo [34] and the other rows were not quoted by them.

n	op	$\langle \mathrm{LS}\|$	$\|\mathrm{LS}'\rangle$	`qlanth`	fncross
3	$\hat{t}_7$	${}^2\mathrm{L}$	${}^2\mathrm{L}$	−0.026503	−0.026053
6	$\hat{t}_4$	${}^1\mathrm{S1}$	${}^1\mathrm{S3}$	5.737097	−5.737097
6	$\hat{t}_4$	${}^1\mathrm{Q}$	${}^1\mathrm{Q}$	−0.856893	0.000000
7	$\hat{t}_3$	${}^2\mathrm{F1}$	${}^2\mathrm{F8}$	−4.535574	−3.239695
8	$\hat{t}_3$	${}^1\mathrm{S1}$	${}^1\mathrm{S3}$	−5.7371	5.7371
8	$\hat{t}_6$	${}^1\mathrm{S2}$	${}^1\mathrm{S3}$	−3.55842	3.55842
8	$\hat{t}_7$	${}^1\mathrm{S3}$	${}^1\mathrm{S4}$	2.53546	−2.53546
8	$\hat{t}_2$	${}^1\mathrm{S2}$	${}^1\mathrm{S3}$	−0.589802	−1.4863
8	$\hat{t}_4$	${}^1\mathrm{Q}$	${}^1\mathrm{Q}$	0.856893	0.0
8	$\hat{t}_4$	${}^1\mathrm{S3}$	${}^1\mathrm{S4}$	−0.29277	0.29277
12	$\hat{t}_2$	${}^1\mathrm{G}$	${}^1\mathrm{G}$	−0.404061	0.000000

dealing with the $\hat{m}_{(k)}$ and $\hat{p}_{(k)}$ operators that are not orthogonal [40,64].

We would like to highlight the special case of the f^{12} configuration (Tm^{3+}), because it has been a point of misunderstanding and errors in past results. Some matrix elements $\langle\psi_i|\hat{t}_2|\psi_j\rangle_{f^{12}}$ of the non-orthogonal operator $\hat{t}_2$ are nonzero; this is confusing since a three-body term is then present in f^{12}, which is a complementary configuration of two holes. On the contrary, if one uses $\hat{t}_2^{\perp}$ then all matrix elements $\langle\psi_i|\hat{t}_2^{\perp}|\psi_j\rangle_{f^{12}}$ are zero, and, as such, the energy spectrum of Tm^{3+} is independent of the parameter $T_{\perp}^{(2)}$.

III. QUANTITATIVE COMPARISONS WITH THE LITERATURE

In this section, we will provide a quantitative comparison between results from `qlanth` and the results presented by Carnall *et al.* for LaF_3 in Ref. [21]. We will point to errors in the spectroscopic tables and additional features that allowed us to reproduce, fairly closely, their results by reintroducing known and additional errors.

A. Errors in the spectroscopic tables of reduced matrix elements

In 2008, Chen *et al.* [33] reported errors in the tabulated values of the reduced matrix elements of the spin-other-orbit coupling $\hat{m}_k$ and the electrostatically correlated spin-orbit interaction $\hat{p}_k$. As Chen *et al.* described, errors were found in data files with tabulated reduced matrix elements, which we refer to as *fncross* tables, a naming consistent with prior works, in recognition of the foundational work of Judd, Crosswhite, and Crosswhite [40] that first produced these tables. These tables have been used in several codes including SPECTRA (supported by the Argonne National Laboratory [65]) and *linuxemp*, and our results indicate that these tables were also used by Carnall *et al.* [21].

In addition to the errors mentioned above, Judd and Lo [34] identified errors in the reduced matrix elements of the three-electron configuration-interaction $\hat{t}_k$. We extracted the *fncross* tables from Ref. [66], where there are two alternatives for the *fncross* tables: *fn* and *fn_new*. The *fn_new* files fix the errors identified by Chen *et al.*, but still contain the errors identified by Judd and Lo. Furthermore, we found that the *fncross* tables (*fn* and *fn_new*) contain a few additional errors in the $\hat{t}_k$ matrix elements, listed in Table II. Finally, for $N = 7$, there is a typo in Judd and Lo, where $\langle {}^2\mathrm{F5}|\hat{t}_3|{}^2\mathrm{F8}\rangle$ should be $\langle {}^2\mathrm{F1}|\hat{t}_3|{}^2\mathrm{F8}\rangle$. Furthermore, when the method of fractional parentage is used to calculate reduced matrix elements for all f^N, some matrix elements that are exactly zero when computed with symbolic arithmetic (as done here) may yield small but nonzero values because of accumulated rounding error when using finite precision arithmetic (see the Supplemental Material, SM [67] for a complete list of errors).

The results presented below make us believe that the errors pointed above were present in the calculations performed by Carnall *et al.* [21]. In Fig. 1, we compare the calculated energies using `qlanth` and those quoted by Carnall *et al.* for the cases when errors are included in the calculation and when they are not. We clearly see that the calculated energies are much closer to theirs when the errors are present. These errors can lead to differences in the energy spectrum of approximately $\sim 30\,\mathrm{cm}^{-1}$, as observed for erbium. Across all lanthanide ions, we find an average discrepancy of about $10\,\mathrm{cm}^{-1}$, which is significantly larger than the nominal $1\,\mathrm{cm}^{-1}$ uncertainty typically reported for experimental values.

B. Omission of the spin-spin interaction

Beyond the errors discussed above, we noticed that some of the remaining discrepancies in Fig. 1 can be reduced by excluding the spin-spin contribution $\hat{m}_k^{s\text{-}s}$ to the Marvin integrals. Whereas Carnall *et al.* [21] claim to have included the spin-spin contribution to the magnetic interactions present in the spectrum, our calculations indicate that this term was omitted. In Fig. 2, we compare the calculated energies using `qlanth` and those quoted by Carnall *et al.* for the cases when the spin-spin contribution is included in the calculation and when it is not. Again, we clearly see that the calculated energies are much closer to reported values when the spin-spin contribution is absent. Notice that in this figure all the results include the errors discussed in the previous subsection. Also, the effect of excluding the spin-spin contribution brings the differences down to $5\,\mathrm{cm}^{-1}$ or less. Finally, we would like to stress that removing the spin-spin contribution was only done with the intent of understanding the calculations in Ref. [21]; thus, except for the results in Fig. 2, all other results presented here include this term. Finally, the spin-spin contribution is

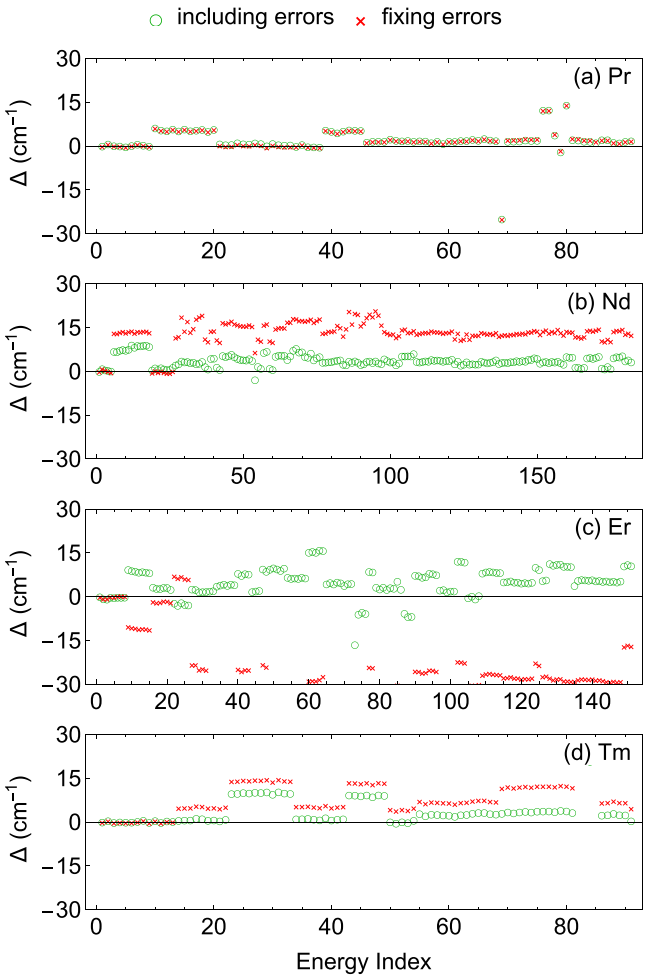

FIG. 1. Differences ($\Delta \equiv E_{ql} - E_R$) between the energies calculated using `qlanth` (E_{ql}) and those quoted by Carnall *et al.* in Ref. [21] (E_R) for the cases when the errors discussed in Sec. III are included (green circle) and when they are not (red cross). In these differences, both sets of energies are shifted to share a common energy for the ground state.

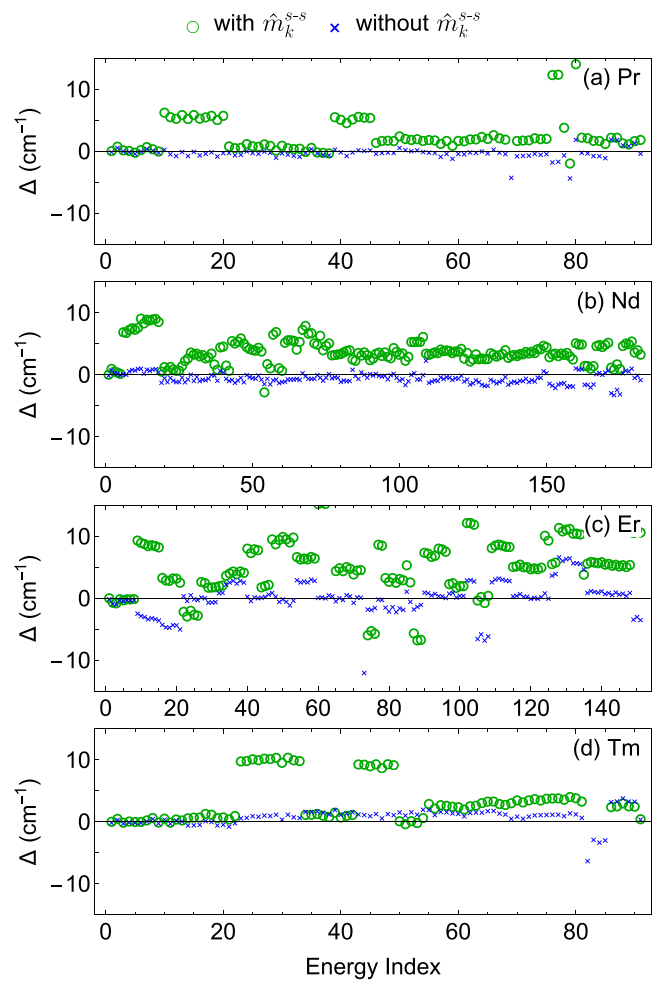

FIG. 2. Differences ($\Delta \equiv E_{ql} - E_R$) between the energies calculated using `qlanth` (E_{ql}) and those quoted by Carnall *et al.* in Ref. [21] (E_R) for the cases when the Hamiltonian term $\hat{m}_k^{s\text{-}s}$ is included (green circle) and when it is excluded (blue cross). These results include the errors discussed in Sec. III, thus the green circles are the same data as in Fig. 1.

zero in the multiplets with $S = 0$ and is independent (as long as J is a good quantum number) of M_J, that explains the plateaus in the energy differences.

For completeness and clarity, in Fig. 3 we present a comparison between our best attempt at reproducing the energy spectra reported by Carnall *et al.* [21] (blue cross in Fig. 2) and the results that we obtained after correcting the errors (red cross in Fig. 1)—notice that in Figs. 1–3, each spectra (E_{ql} and E_R) is shifted to have a zero ground-state energy, in this way Δ always starts at zero value for the first energy index. In that figure, the blue crosses show that we were able to reproduce the calculations of Carnall *et al.* [21] for most ions with a precision of a few cm^{-1}. The most striking difference is for Tb^{3+}, where a discrepancy of $\sim 30\,\mathrm{cm}^{-1}$ is observed across the spectrum. Sm and Dy also show some large deviations from their results. On the other hand, the red crosses indicate that in many cases the correct calculations are noticeably different, with the most notable case being the Er ion, which consistently shows deviations of $\sim 30\,\mathrm{cm}^{-1}$.

C. Typographical mistakes in quoted energy levels

In the appendix of Ref. [21], we have found a few obvious typographical errors. We detail them in the SM [67]. Furthermore, the tables sometimes report only the number of energy levels within a certain range, instead of listing the explicit values; other times they report a gap in the spectrum at high energies. In a few cases, we found these ranges incompatible with calculations. For these reasons, we have included in the supplementary electronic files, the adjusted list of energies that we used to compare the results presented here.

D. Other codes

We performed an extensive analysis of our results with two other available codes. Specifically, we have made comparisons against *Lanthanide* authored by Edvardsson and Åberg [68], and *linuxemp* by Reid [66].

The comparisons were established through the energy spectra, generated from different codes using the same set

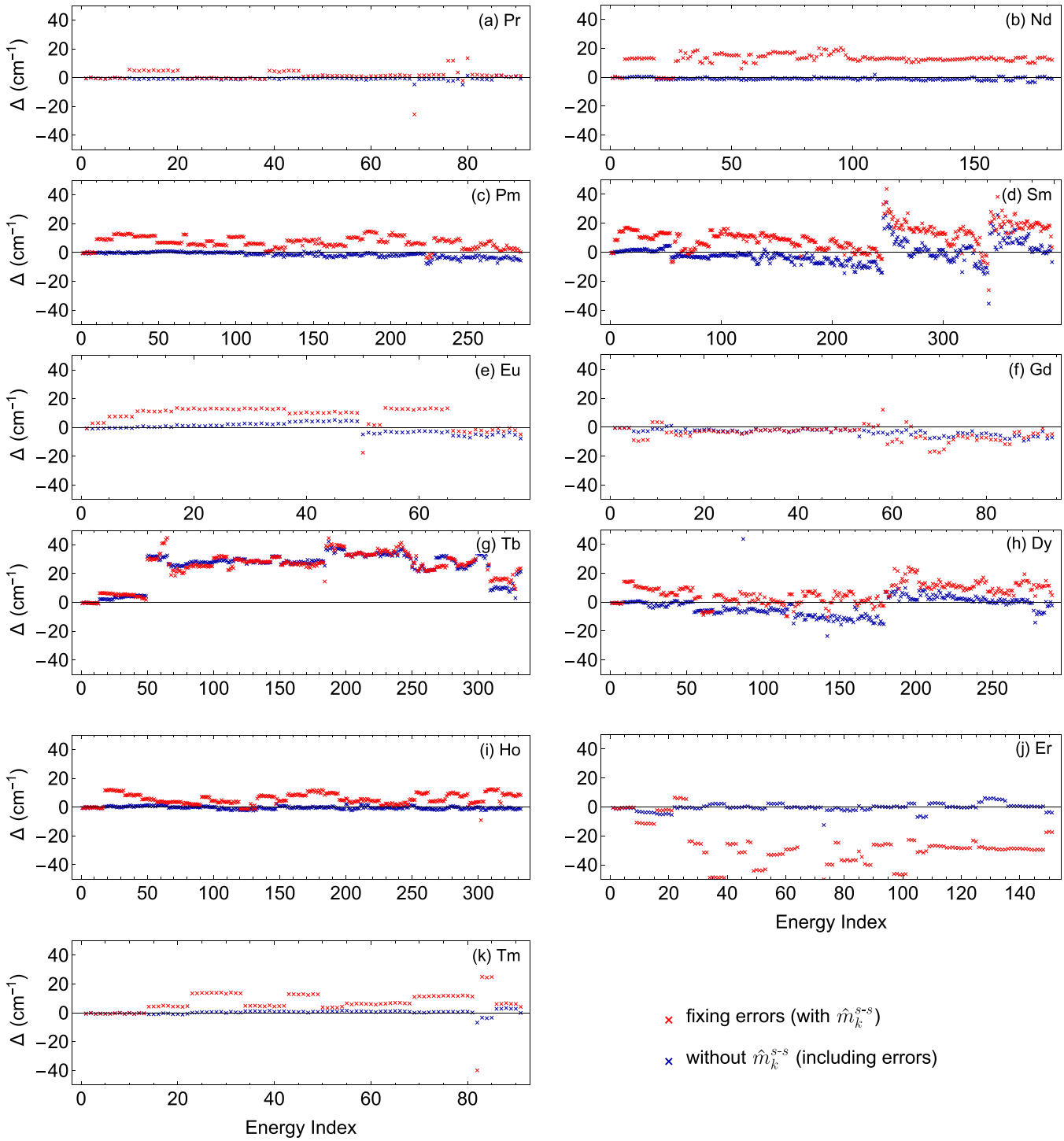

FIG. 3. Differences ($\Delta \equiv E_{ql} - E_R$) between the energies calculated using `qlanth` (E_{ql}) and those quoted by Carnall *et al.* in Ref. [21] (E_R) for the case when the errors discussed in Sec. III are corrected and the Hamiltonian term $\hat{m}_k^{s\text{-}s}$ is included (red cross), and for the case when errors discussed in Sec. III are included in the calculation and the Hamiltonian term $\hat{m}_k^{s\text{-}s}$ is excluded (blue cross).

of parameters. First, it is important to note some substantial differences between codes. For instance, *Lanthanide* does not include $M^{(k)}$ or $P^{(k)}$ parameters; therefore, we set those parameters to zero in these calculations. Overall, we found that `qlanth` and *Lanthanide* have an excellent numerical agreement (up to 10^{-7}) only if the $T^{(k)}$ parameters are set to zero in the calculations. On the other hand, calculations with a complete set of parameters, including $T^{(k)}$, show significant differences in the spectra. Unfortunately, we could not resolve or find an intuitive explanation for these differences. More details of these results are provided in the set of electronic files.

In the case of *linuxemp*, we used a publicly available version from 2018 [66]. This included two alternatives for the *fncross* tables, including the latest one with fixes to the errors

identified by Chen *et al.* [33]. For comparison, we omitted the spin-spin contribution (which is also excluded in *linuxemp* as per their documentation) and used the most recent version of the *fncross* tables in *linuxemp*, keeping the same parameters to calculate energies with both codes. In most cases the maximum absolute difference between the two sets of calculated energies (for the entire calculated energy spectra) was found to be smaller than $0.2\,\mathrm{cm}^{-1}$. Exceptionally, in the cases of Eu, Gd, Tb, and Tm, the maximum absolute differences were $680\,\mathrm{cm}^{-1}$, $32\,\mathrm{cm}^{-1}$, $560\,\mathrm{cm}^{-1}$, and $94\,\mathrm{cm}^{-1}$, respectively. If the mean of the absolute differences is considered, then in all cases (excluding Tm, in which it is $16\,\mathrm{cm}^{-1}$) the mean discrepancies are always smaller than $3\,\mathrm{cm}^{-1}$, which tells us that most of the energies were similar with a few exceptions. We have identified that the outlier energies that give the large maximum discrepancies are the result of the additional errors identified in Table II. Accounting for these errors, the maximum absolute differences drop to below $1.1\,\mathrm{cm}^{-1}$ in all cases. Since *linuxemp* is widely used, we provide corrected versions of the *fncross* files in the SM [67].

After extensive comparisons with the codes mentioned above, we also came across other relevant codes. These include `pycf` by Sebastian Horvath [69], `Dicke` by Jevon Longdell [70], and most recently `NJA-CFS` code by Fiorucci and Ravera [71,72]. Comparing our results to these would be an interesting avenue for future work.

IV. UPDATED LEVEL STRUCTURES

In this section we show our results of the refitted parameters of the semi-empirical Hamiltonian for the case of lanthanide ions in LaF_3. Specifically, Table III shows our obtained parameters when the model is fitted to the same energy levels used in Carnall *et al.* [21]. In these calculations, we have included the spin-spin contribution term $\hat{m}_k^{s\text{-}s}$ and corrected the errors discussed in Sec. III. The assumptions for these calculations are described below in detail and reflect our best effort to reproduce the parameter choices in that reference.

A. Fitting assumptions

First, our fittings to the model parameters use the same experimental energy levels used in Ref. [21] for LaF_3. Second, previous numerical approaches used a truncated version of the semi-empirical Hamiltonian in the fitting procedure (although the full diagonalization is made with the converged parameters to obtain the final energy spectrum); here, truncation was completely avoided, see the SM [67] for more details. Third, when some parameters are constrained as proportional to others, we kept the same ratios as Carnall *et al.* [21]. Specifically, for Eu we fixed $F^{(4)} = 0.713F^{(2)}$ and $F^{(6)} = 0.512F^{(2)}$; for Gd we fixed $F^{(4)} = 0.71F^{(2)}$; and for Tb we fixed $F^{(4)} = 0.707F^{(2)}$. For the $M^{(k)}$ and $P^{(k)}$ parameters we used the constraints $M^{(2)} = 0.56M^{(0)}$, $M^{(4)} = 0.31M^{(0)}$, $P^{(4)} = 0.5P^{(2)}$, and $P^{(6)} = 0.1P^{(2)}$ for all ions. Fourth, since Carnall *et al.* held some parameters fixed, we repeated this pattern (see Table III). Fifth, we also assumed a C_{2v} site symmetry for the crystal field.

In Carnall *et al.* [21], ad hoc choices were made for some parameters that were held fixed with the intent of improving the fitting. Instead of addressing these small improvements individually, we chose to implement a systematic protocol as explained in the following. When a parameter is held fixed for a given lanthanide, previously fitted values in other lanthanides are used to decide the value at which it is fixed during fitting. We notice that for Pr, Nd, and Dy every parameter is freely varied, so we used those three cases as starting points. From there, we used a linear fit (number of electrons in the f shell versus parameter value) to fix the parameter values for Ce and Sm. For example, a linear fit from the $B_2^{(2)}$ parameters from Pr, Nd, and Dy [(2, −126), (3, −50), and (9, −60)] allowed us to extrapolate/interpolate and obtain the values for Ce and Sm [(1, −98) and (5, −80)]. We followed this procedure in the following sequence: Ce → Sm → Ho → Er → Tm → Yb → Tb → Eu → Gd. In this sequence, whenever a parameter is to be held fixed for a given lanthanide, the previously fitted values are considered. For example, the $B_0^{(2)} = -224\,\mathrm{cm}^{-1}$ parameter in Ho was obtained from a linear fit from Pr, Nd, Dy, and Sm [notice

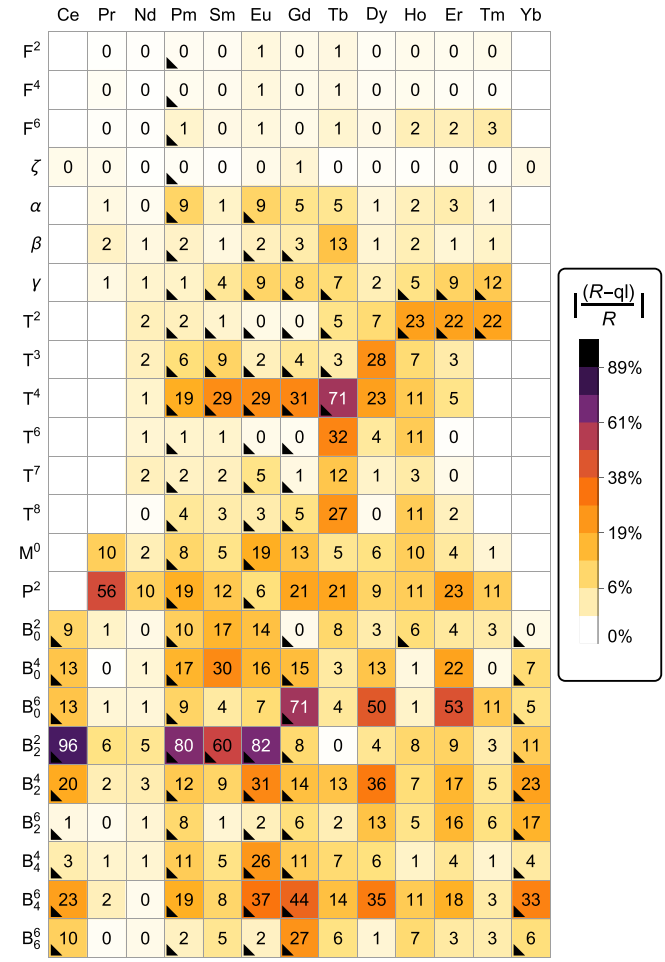

FIG. 4. Relative absolute differences (%) between the fitted parameters shown in Table III (ql) and those quoted by Carnall *et al.* in Ref. [21] (R). The colors represent the intensity of these percentage differences according to the scale bar on the right and, for better visualization, we also write the calculated values on their corresponding squares. Empty squares, not numbered, indicate parameters that are not present in the model.

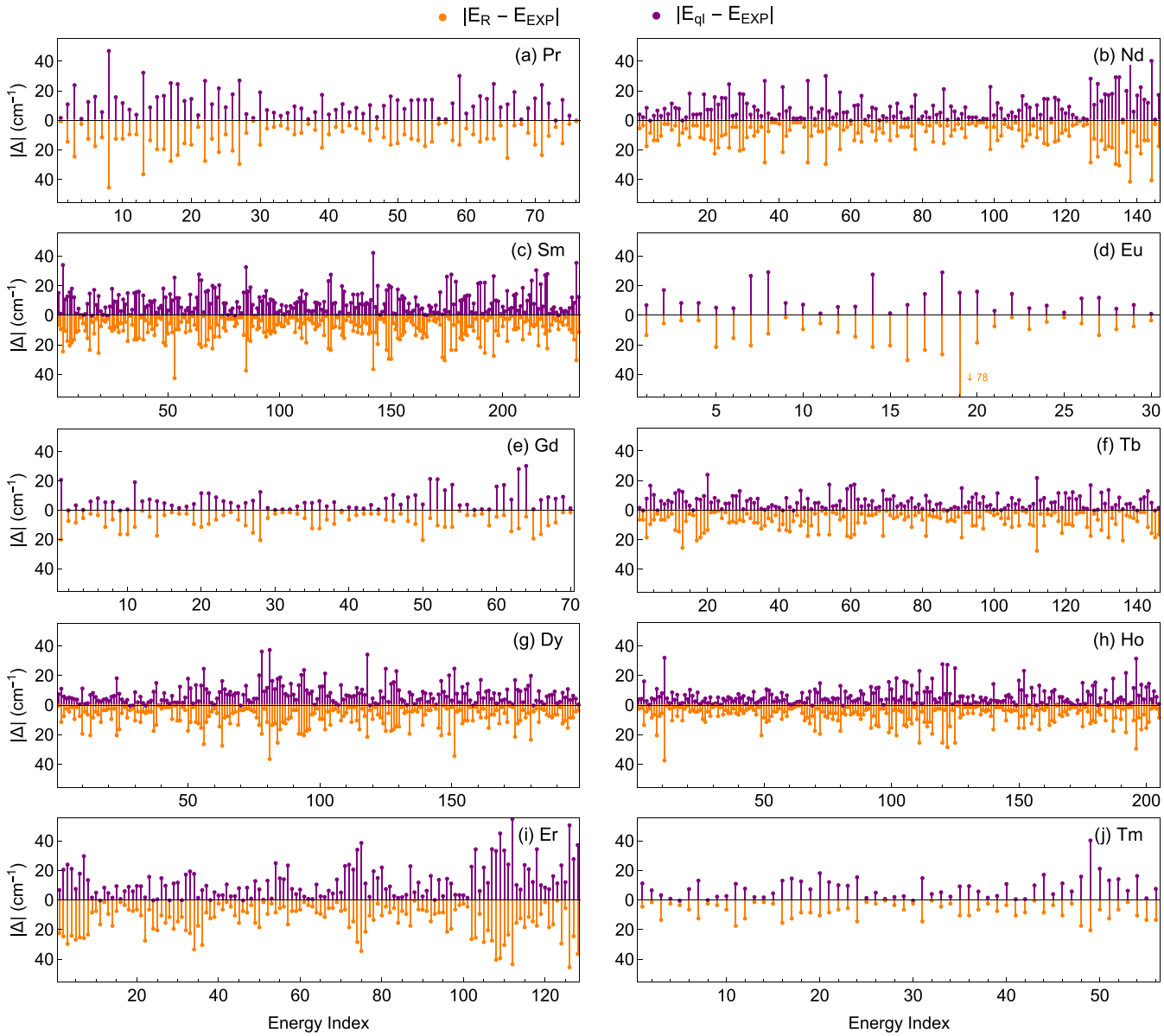

FIG. 5. Absolute differences between calculated values with refitted parameters and experimental data. The upper axis (purple color online) shows the difference between our calculated values and the experimental ones. The lower axis (orange color online), shows the differences between the values reported by Carnall *et al.* and the same experimental ones.

that we have not used $B_0^{(2)}$ from Ce, because in that case $B_0^{(2)}$ was fixed and not freely varied]. The $F^{(k)}$ and ζ parameters are exceptions to the linear fit, these parameters have a non-linear trend across the lanthanide row. For these parameters, we took an empirical approach and used a cubic spline interpolation based on previously fit values. A common practice is using $\zeta \propto Z^2$ [73], where Z is the atomic number. This order was motivated by the number of estimated parameters needed and number of experimental values available.

The above paragraph describes our best approach to reproduce the approach to fitting used by Carnall *et al.* [21]. However, we acknowledge that different approaches could further improve the fitting process. For instance, we believe the parameters follow a trend across the lanthanide series, making a global fit—fitting the parameters for all lanthanides simultaneously—a more suitable approach. This could involve imposing a simple relationship between the parameters and reducing their overall number of independent variables. Lastly, an additional improvement may be achieved in considering a crystal field with C_2 site symmetry—the actual symmetry of the La sites in LaF_3.

B. Fitting method and uncertainties

Following the approach of Carnall *et al.* [21], we used the Levenberg-Marquardt method [74,75] to find parameter values that minimize $s^2 = \sum_i (E_{\rm ql} - E_{\rm EXP})_i^2$. This is a deterministic fitting method, that requires an initial guess to parameter values, so we use the parameters in Ref. [21] as starting points. As such, the fitted parameters here reflect a

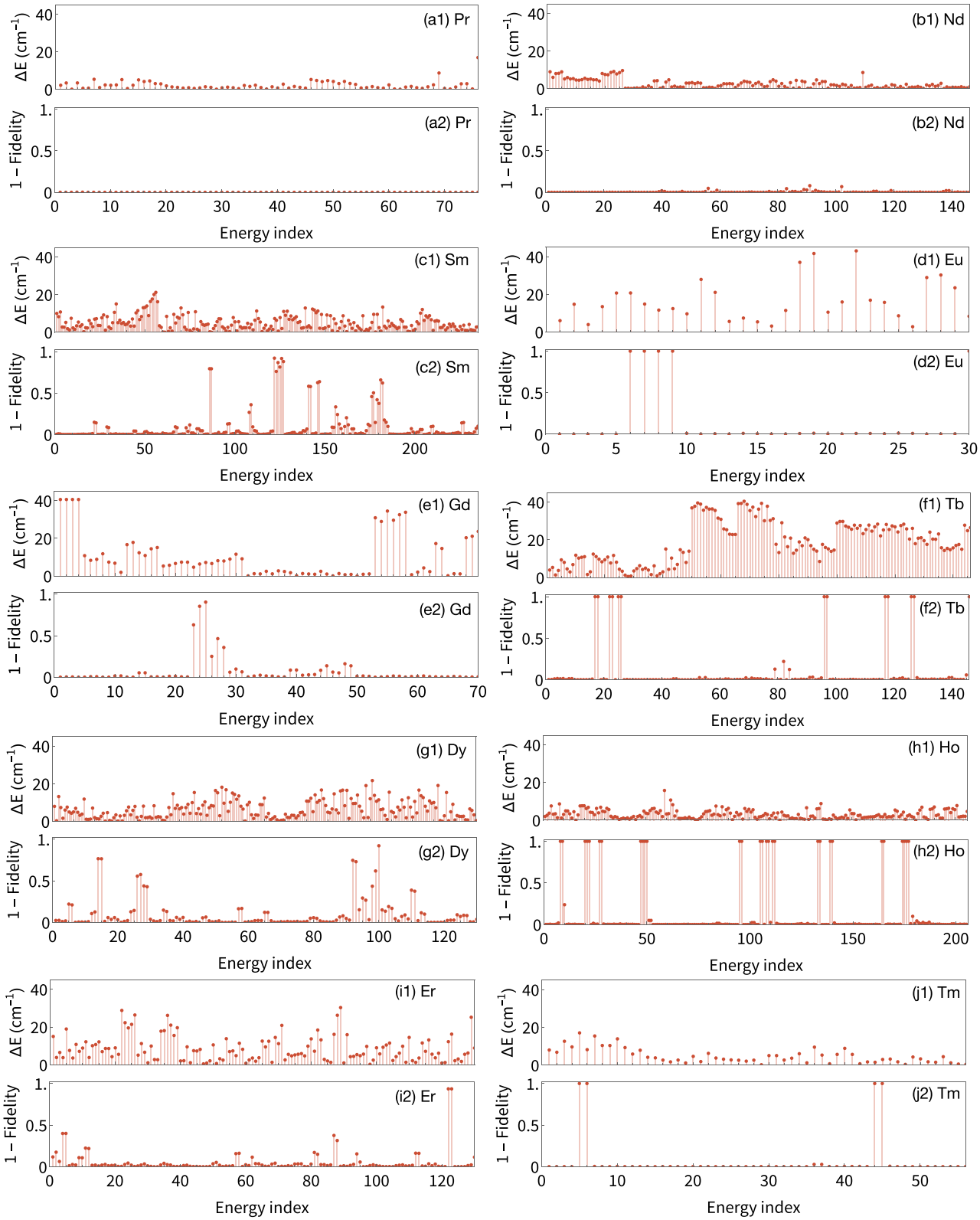

FIG. 6. (x1) Energy difference, $\Delta E = |E_R - E_{ql}|$, and (x2) fidelity, $(\mathrm{Tr}\sqrt{\sqrt{\rho_{\mathrm{ql}}}\rho_R\sqrt{\rho_{\mathrm{ql}}}})^2$, between the eigenvectors for lanthanide ions in LaF_3, computed using the parameters in Table III and the parameters reported in Carnall *et al.* [21].

refinement of those results, rather than an attempt to find global minima; see discussion in Appendix C.

For obtaining the uncertainties, the specific parametric form of the semi-empirical Hamiltonian allows one to compute the gradient of each energy i as a function of the parameters $E_i(\{\boldsymbol{p}\}) = E_i^0 + \nabla E_i \cdot (\boldsymbol{p}_0 - \boldsymbol{p})$, where $\boldsymbol{p}$ comprises the set of parameters involved in the fitting. This method yields ∇E_i from a simple re-interpretation of terms

in first-order perturbation theory. This linear approximation of the eigenvalues around the local minimum then allows one to compute s^2 to second order in the model parameters $\boldsymbol{p}$. Here, a constant uncertainty in the energy differences was assumed to be $1\,\mathrm{cm}^{-1}$. This is compatible with the nominal uncertainty of the energies in Ref. [21], and provides uncertainties in the parameters that are of similar magnitude to the ones provided by them. Together with the number of degrees of freedom ν in the corresponding fit, this allows us to compute the error intervals from the contour $\tilde{\chi}^2 = \frac{1}{\nu}\frac{s^2}{\sigma_{\mathrm{exp}}^2} = \tilde{\chi}^2_{\mathrm{min}} + 1$ [76].

C. Fitted parameters and energy spectrum

Our main results are summarized in Table III, which shows fitted parameters for LaF_3 (see SM [67] for an equivalent analysis of $LiYF_4$). Analyzing these results, we find that the average root mean squared deviation (σ) in our calculation is similar to those (σ_{Ref}) in Ref. [21], despite the significant differences in some parameters. Figure 4 shows the percentage differences between fitted parameters. Investigating the results in this figure, we notice that the Coulomb interaction $F^{(2)}$, $F^{(4)}$, $F^{(6)}$, and the spin-orbit ζ parameters do not show a significant change with respect to the reference values. The two-electron configuration-interaction parameters α, β, and γ show small relative differences ($\lesssim$10%). This is understandable because these parameters (for which there are no significant errors in Carnall *et al.* [21]) set the general structure of the spectrum. Larger differences (about 30% or higher) appear in the three-electron configuration-interaction $T^{(k)}$ and the pseudomagnetic $P^{(k)}$ parameters. Interestingly, $T^{(2)}$ parameters become significantly different above $N = 7$ electrons and the $T^{(4)}$ parameter have the largest relative differences, across the lanthanide row. The crystal field parameters $B_q^{(k)}$ are generically different, with the exception of Pr and Nd ions that show very good agreement. In fact, all Nd fitted parameters are very close to the reference results.

Figure 5 compares the difference between the reported calculated energies and experimental values in Carnall *et al.* [21] with our fit results that include all the corrections noted above. Note that the residuals between the fitted energies and the experimental values in Fig. 5 are $\sim 10\,\mathrm{cm}^{-1}$. Quantitatively, this agrees with the root mean square error (σ) of $8\,\mathrm{cm}^{-1}$ to $19\,\mathrm{cm}^{-1}$ shown in Table III, except in the cases of Ce and Yb, which have exceptionally large σ because of the large number of parameters in comparison with the number of available energy levels. Relatedly, we notice that the Pr, Eu, Gd, and Tm ions present less than 100 energies for the fitting; in the case of Eu there are only $\sim$30 energies, which can be the reason for the large differences in the resulting parameters, as shown in Fig. 4.

D. Comparison between eigenvectors

Besides comparing the energies calculated using different approaches, it is also worthwhile to compare the resulting eigenvectors, as they reflect errors in propagated quantities such as transition rates.

We use fidelity (F) to quantify the difference between states, defined as $F = (\mathrm{Tr}\sqrt{\sqrt{\rho_1}\rho_2\sqrt{\rho_1}})^2$. For an odd number of electrons in the $4f^N$ shell, it is necessary to consider both states of the degenerate Kramers pair ($|\psi\rangle$ and $|\psi_K\rangle$) in order to adequately compare the results. In these cases, we employ the maximally mixed state to compare subspaces, i.e., $\rho = 1/2(|\psi\rangle\langle\psi| + |\psi_K\rangle\langle\psi_K|)$. For an even number of electrons, the fidelity simplifies to $F = |\langle\psi_1|\psi_2\rangle|^2$. The states are identical when $F = 1$ and orthogonal when $F = 0$.

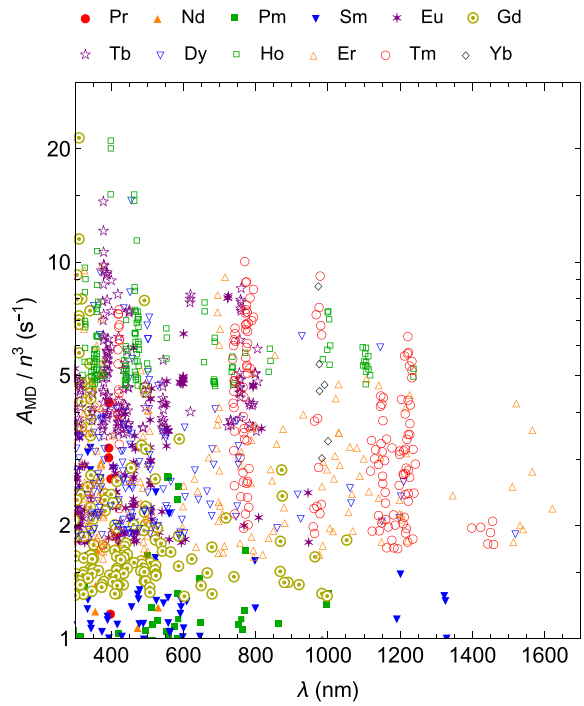

FIG. 7. Calculated magnetic dipole transition rates A_{MD}/n^3 of the lanthanide ions in LaF_3 for transitions from ultraviolet to infrared. All data provided in the electronic files.

Figure 6 compares the fidelity between the states obtained with `qlanth` using the refined parameters from Table III with those from our best attempt to reproduce the results from Carnall *et al.* [21], as described in Sec. III (i.e., putting back the errors in the matrix elements and excluding the spin-spin contribution). Two extreme cases are observed: significant differences in the energies having almost identical states ($F = 1$), as well as similar energies having fidelities noticeably smaller than 1. A good example is Pr, for which all eigenvectors are nearly identical, showing that two distinct spectra can describe essentially the same states. As a counterexample, Ho illustrates that similar energies can correspond to very different states. Furthermore, in most cases, the ground state and the first few excited states are nearly identical, with the notable exception of Er, which exhibits significantly different states in the ground state ($F = 0.88$). Overall, these results highlight that errors in the Hamiltonian can be compensated by the fitted parameters, yielding energy spectra that appear equally accurate to experimental data, but at the cost of producing errors in the eigenvectors, as illustrated in this figure.

V. MAGNETIC DIPOLE TRANSITIONS

In this section we discuss the absorption and emission rates for magnetic dipole transitions [77] and show results for the

FIG. 8. Maximum magnetic dipole transition rates for different wavelength ranges across the lanthanide ions. The height of the bar indicates the magnitude of the rate and the text shows the main $(2S+1)LJ$ component of the initial and final states. Cases marked with * are cases in which the given coarse labels are ambiguous, see Table IV for a longer description of these cases.

TABLE III. Fitted model parameters using `qlanth`. Following Carnall *et al.* [21], parameters in square brackets were held fixed during fitting. In the case of Eu, Gd, and Tb, some Slater parameters were constrained to be proportional to $F^{(2)}$. For Eu, $F^{(4)} = 0.713F^{(2)}$ and $F^{(6)} = 0.512F^{(2)}$. In the case of Gd, $F^{(4)} = 0.71F^{(2)}$. And in the case of Tb, $F^{(4)} = 0.707F^{(2)}$. The data was fitted in the following order: Pr, Nd, Dy, Ce, Sm, Ho, Er, Tm, Yb, Tb, Eu, Gd.

	Ce	Pr	Nd	Pm	Sm	Eu	Gd	Tb	Dy	Ho	Er	Tm	Yb
F^2		68870(10)	73040(20)	[76501]	79690(20)	82612(7)	85415(10)	88520(60)	91790(80)	94310(50)	97680(20)	100420(10)	
F^4		50410(30)	52790(80)	[55009]	57050(50)	[58902]	[60645]	[62581]	64300(200)	66530(90)	67970(40)	69580(40)	
F^6		32890(20)	35770(40)	[38164]	40080(30)	[42297]	44610(10)	46720(70)	49200(200)	50860(90)	52800(40)	54260(60)	
ζ	645.4(0.4)	749.8(0.8)	885(1)	[1026]	1176(1)	1333.7(0.5)	1493(2)	1707(2)	1911(2)	2144(1)	2378(1)	2633.9(0.5)	2914.6(0.4)
α		16.1(0.1)	21.4(0.1)	[19]	19.9(0.1)	[18]	17.98(0.07)	17.6(0.2)	17.9(0.3)	17.5(0.2)	17.3(0.1)	17.1(0.2)	
β		−558(7)	−590(6)	[−568]	−563(9)	[−578]	[−582]	−510(30)	−630(10)	−622(7)	−588(6)	−615(9)	
γ		1364(6)	1430(10)	[1496]	[1563]	[1630]	[1697]	[1764]	1830(60)	[1898]	[1964]	[2031]	
T^2			292(5)	[294]	[296]	[299]	[301]	[303]	310(10)	[308]	[310]	[313]	
T^3			36(2)	[37]	[39]	[39]	[40]	[41]	46(6)	40(3)	44(3)		
T^4			60(3)	[69]	[72]	[77]	[81]	[85]	100(30)	119(6)	69(3)		
T^6			−288(5)	[−314]	−351(9)	[−301]	[−294]	−270(30)	−330(20)	−230(20)	−271(6)		
T^7			339(7)	[356]	366(8)	[351]	[348]	340(20)	400(10)	330(30)	310(10)		
T^8			305(9)	[333]	338(5)	[329]	[327]	400(10)	316(9)	300(10)	290(10)		
M^0		1.9(0.1)	2.2(0.1)	[2]	2.5(0.1)	[2]	2.8(0.1)	2.5(0.1)	3.2(0.1)	2.3(0.1)	4(0.1)	3.8(0.2)	
P^2		−40(20)	210(30)	[224]	310(30)	[338]	530(60)	450(40)	650(30)	540(30)	730(40)	620(30)	
B_0^2	[−237]	−221(7)	−260(10)	[−220]	−190(20)	−190(10)	[−230]	−250(20)	−240(20)	[−224]	−247(9)	−257(8)	[−250]
B_0^4	[645]	740(20)	500(60)	[551]	320(60)	480(30)	[515]	630(40)	570(50)	560(40)	350(50)	460(20)	[425]
B_0^6	[766]	670(20)	650(40)	[583]	630(60)	520(30)	[479]	290(40)	190(50)	380(40)	570(40)	310(20)	[297]
B_2^2	[−98]	−127(6)	−50(10)	[−90]	[−80]	[−91]	[−92]	−100(10)	−70(10)	−100(10)	−99(9)	−102(5)	[−94]
B_2^4	[518]	420(10)	510(30)	[464]	650(40)	[413]	[388]	300(30)	200(40)	270(30)	360(30)	310(10)	[248]
B_2^6	[−926]	−920(10)	−830(30)	[−809]	−700(40)	[−720]	[−676]	−700(30)	−670(30)	−550(30)	−410(40)	−450(20)	[−398]
B_4^4	[599]	610(10)	570(30)	[543]	430(30)	[514]	[500]	490(30)	550(30)	460(20)	400(30)	430(10)	[413]
B_4^6	[−429]	−360(20)	−410(30)	[−365]	−470(40)	[−318]	[−294]	−230(20)	−150(40)	−200(20)	−200(20)	−240(20)	[−158]
B_6^6	[−866]	−790(20)	−830(30)	[−747]	−720(40)	[−680]	[−647]	−540(30)	−550(30)	−590(20)	−520(30)	−510(20)	[−461]
ε	7	−2	−4		−16	−7	−21	−2	−8	−4	−7	−12	−11
n	7	75	146		233	29	70	146	198	204	127	56	5
σ	46	16	14		13	16	11	8	12	9	19	13	59
nRef	7	75	146		232	29	70	146	198	204	127	56	5
σRef	51	16	14		13	16	10	12	12	10	19	10	38

lanthanides in LaF_3—these calculations expand upon and correct the work from Dodson and Zia [15], wherein specifically, the $T^{(2)}$ parameter was mistakenly omitted for the Tm^{3+} ion and the code contained a typo in the matrix elements from the $\hat{L}^2$ operator. In the following, both absorption and emission are calculated from the line strength defined between any two

TABLE IV. Energies and wavevectors truncated to the largest contributions involved in the spontaneous transitions shown in Fig. 8 marked with *. For each transition, the transition wavelength $\lambda = (E_{\text{initial}} - E_{\text{final}})^{-1}$ is provided together with the initial and final energies, E_{initial} and E_{final}, as well as the corresponding eigenvectors $|\psi_{\text{initial}}\rangle$ and $|\psi_{\text{final}}\rangle$. Contributions to the eigenvectors different only by the sign of M_J are aggregated as $\pm M_J$.

Lanthanide λ(nm)	$E_{\text{initial}}(\text{cm}^{-1})$ $E_{\text{final}}(\text{cm}^{-1})$	$\|\psi_{\text{initial}}\rangle$ $\|\psi_{\text{final}}\rangle$
Eu	55717	$-0.23\|^3\text{M2}_{10,\pm6}\rangle + 0.21\|^3\text{M2}_{10,0}\rangle - 0.20\|^3\text{M3}_{10,\pm6}\rangle - 0.20\|^1\text{N2}_{10,\pm6}\rangle$
948 nm	45168	$+0.22\|^3\text{M3}_{10,\pm5}\rangle - 0.21\|^3\text{O}_{10,\pm5}\rangle$
Eu	80943	$-0.22\|^3\text{M1}_{8,\pm8}\rangle + 0.21\|^3\text{M1}_{8,\pm2}\rangle$
1568 nm	74565	$-0.23\|^3\text{M1}_{8,\pm7}\rangle + 0.17\|^1\text{L4}_{8,\pm7}\rangle$
Dy	46383	$-0.23\|^4\text{P2}_{\frac{5}{2},\frac{5}{2}}\rangle - 0.21\|^2\text{F7}_{\frac{5}{2},\frac{5}{2}}\rangle - 0.17\|^4\text{P2}_{\frac{5}{2},-\frac{3}{2}}\rangle - 0.17\|^4\text{G4}_{\frac{5}{2},\frac{5}{2}}\rangle$
1339 nm	38915	$-0.4\|^4\text{P2}_{\frac{5}{2},-\frac{3}{2}}\rangle - 0.32\|^6\text{P}_{\frac{5}{2},-\frac{3}{2}}\rangle + 0.28\|^4\text{G1}_{\frac{5}{2},-\frac{3}{2}}\rangle + 0.28\|^4\text{G4}_{\frac{5}{2},-\frac{3}{2}}\rangle$
Dy	46477	$+0.21\|^4\text{P2}_{\frac{5}{2},\frac{3}{2}}\rangle - 0.21\|^4\text{P2}_{\frac{5}{2},-\frac{5}{2}}\rangle + 0.20\|^4\text{I2}_{\frac{9}{2},-\frac{1}{2}}\rangle + 0.19\|^2\text{F7}_{\frac{5}{2},\frac{3}{2}}\rangle - 0.19\|^2\text{F7}_{\frac{5}{2},-\frac{5}{2}}\rangle$
1352 nm	39078	$+0.39\|^4\text{P2}_{\frac{5}{2},-\frac{5}{2}}\rangle + 0.31\|^6\text{P}_{\frac{5}{2},-\frac{5}{2}}\rangle - 0.28\|^4\text{G1}_{\frac{5}{2},-\frac{5}{2}}\rangle - 0.28\|^4\text{G4}_{\frac{5}{2},-\frac{5}{2}}\rangle$
Ho	41651	$+0.43\|^5\text{D}_{4,0}\rangle - 0.36\|^3\text{F2}_{4,0}\rangle + 0.31\|^3\text{F4}_{4,0}\rangle - 0.27\|^5\text{D}_{4,\pm2}\rangle$
1792 nm	36071	$+0.33\|^5\text{D}_{4,1}\rangle - 0.33\|^5\text{D}_{4,-1}\rangle + 0.24\|^3\text{H4}_{4,1}\rangle - 0.24\|^3\text{H4}_{4,-1}\rangle$

energy levels as

$$\hat{S}(\phi_i, \phi_f) = |\langle \phi_i | \hat{\boldsymbol{\mu}} | \phi_f \rangle|^2, \tag{3}$$

where $\hat{\boldsymbol{\mu}} = -\mu_B(\hat{\boldsymbol{L}} + g_s\hat{\boldsymbol{S}})$ is the magnetic dipole operator and ϕ_i, ϕ_f are the corresponding wavevector of the energy levels E_i, E_f. The spontaneous emission rate is given (in units of s^{-1}) by

$$\frac{A_{\mathrm{MD}}(\phi_i, \phi_f)}{n^3} = \frac{16\pi^3\mu_0\hat{S}(\phi_i, \phi_f)}{3h\lambda^3 g_i}, \quad \text{with } E_i > E_f \tag{4}$$

where $\lambda = hc/|E_i - E_f|$ is the vacuum-equivalent wavelength of the transition, g_i is the degeneracy of the highest energy level, and n is the refraction index of the host material. The oscillator strength is computed as

$$\frac{f_{\mathrm{MD}}(\phi_i, \phi_f)}{n} = \frac{8\pi^2 m_e\hat{S}(\phi_i, \phi_f)}{3hce^2\lambda g_i}, \quad \text{with } E_i < E_f, \tag{5}$$

where g_i is the degeneracy of the lowest-energy level. μ_0, h, m_e, c, and e are fundamental physical constants.

Figure 7 shows the ultraviolet to near-infrared spontaneous emission rates above 1/s for all lanthanides in LaF_3. The energies involved in each transition are not shown; however, the complete information is included in the attached electronic files. It is interesting to notice that the largest transition rates happen for $N \geqslant 7$ (hollow symbols), thus from Gd to Yb in the lanthanide row. These results are comparable to previous free-ion calculations of MD emission rates in the lanthanides [15], but here the rates are calculated for transitions between pairs of individual crystal-field states.

In Fig. 8, we provide more details of some transitions by showing only the largest transition rate within wavelength intervals. In this figure, the bars represent the transition rate and carry coarse labels representing the states involved in that transition. The coarse label shows only the largest contribution to the eigenvector, using $(2S+1)LJ$ notation and the M_J is omitted. Notice that the left column contains the lanthanide ions that have integer spins, while the right column shows the ions with half-integer spins. Of particular interest is the case of Er around 1540 nm transition. Our calculations show that the important transition $^4\mathrm{I}_{15/2} \rightarrow {}^4\mathrm{I}_{13/2}$ at the telecommunication band, with $\lambda = 1543.28$ nm, has $A_{\mathrm{MD}}/n^3 = 4.56\ \mathrm{s}^{-1}$ (comparable to erbium-doped LaF_3 transparent gel [78]).

Table IV shows in detail the energies and eigenvectors involved in some of the spontaneous emissions shown above. Specifically, we show those cases in which the transitions occur between energy states that differ only by their M_J component.

VI. CONCLUSIONS

This work reviews in detail the calculation of the energy spectra and wavefunctions of trivalent lanthanide ions in crystal hosts using the semi-empirical Hamiltonian. We review the theoretical path that transforms the Hamiltonian from the notation of solid-state physics (see Appendix A) to the form finally used for calculations. This form is limited to the ground configuration of $4f$ electrons, although it also includes configuration-interaction corrections. We integrate into our analysis data gathered from previous literature [21,33,34,40,41,79].

We detail the computational challenges encountered in replicating a canonical paper on lanthanide spectroscopy and provide an open-source code, `qlanth`, to ensure reproducibility. This code offers the Hamiltonian representation in both orthogonal and non-orthogonal parameters. It can calculate magnetic dipole line strengths and transition rates, and it also goes beyond the scope of this work to implement the Judd-Ofelt approach for forced electric dipole transitions. Additionally, it has the ability to include or exclude the spin-spin contribution, and enable or disable the errors in spectroscopic tables [33].

Updated calculations were compared against those from Carnall *et al.* [21], clarifying some of their implicit assumptions and finding some additional errors in widely used spectroscopic tables. In particular, our results suggest that the spin-spin dipolar interaction between f electrons was omitted from their calculations, despite their claim of having included it. We also compared our results against other codes [66,68]. Lastly, we provided an updated version of the description of lanthanide ions in LaF_3, as well as providing exhaustive data describing magnetic dipole transitions across the lanthanide row.

In the past decade, experimental advancements have enabled increasingly detailed observation and manipulation of lanthanide ions in crystals, from the coherent control and optical readout of single ions [80] to addressing nuclear spins with coherence times extending into hours [81], as well as refined descriptions of their hyperfine structure [82]. Given that the semi-empirical Hamiltonian plays a central role in the theoretical description of these phenomena and considering that necessary computational details are required for its actual usage, this work offers a computational foothold for future research involving lanthanide ions.

ACKNOWLEDGMENTS

We are grateful to Christopher M. Dodson for useful discussions and sharing iterations of his prior calculations, as well as to Lee Basssett for his insightful feedback. This paper and the development of `qlanth` were supported by the National Science Foundation through Grants No. DMR-1921877 and No. DMR-1922025.

DATA AVAILABILITY

The data supporting this study's findings are available in the Supplemental Material [67] or from the authors upon reasonable request.

APPENDIX A: HAMILTONIAN

A fundamental description of the electromagnetic interactions for the f electrons of lanthanide ions embedded in a crystal host may be represented by the Hamiltonian in Eq. (1), repeated here for convenience,

$$\begin{aligned}\mathcal{H} = {} & \mathcal{H}_{\mathrm{K}} + \mathcal{H}_{\mathrm{n}} + \mathcal{H}_{e\text{-}e} + \mathcal{H}_{\mathrm{s\text{-}o}} \\ & + \mathcal{H}_{\mathrm{s\text{-}s}} + \mathcal{H}_{\mathrm{o\text{-}o}} + \mathcal{H}_{\mathrm{s\text{-}o\text{-}o}} + \mathcal{H}_{\mathrm{CF}}.\end{aligned} \tag{A1}$$

The main contributions are the kinetic (K), nuclear (n), Coulomb (*e*-*e*), and spin-orbit (s-o) terms. In solid-state-physics notation, these are given in the operator form as

$$\mathcal{H}_{\mathrm{K}} = -\frac{1}{2}\sum_i \nabla_i^2, \tag{A2}$$

$$\mathcal{H}_{\mathrm{n}} \approx -\sum_i \frac{Z_{\mathrm{eff}}}{r_i}, \tag{A3}$$

$$\mathcal{H}_{e\text{-}e} = \sum_{i>j} \frac{1}{r_{ij}}, \tag{A4}$$

$$\mathcal{H}_{\mathrm{s\text{-}o}} = \frac{\alpha^2}{2}\sum_i \left(\frac{1}{r_i}\frac{\partial V}{\partial r_i}\right)(\boldsymbol{s}_i \cdot \boldsymbol{l}_i). \tag{A5}$$

In the set of equations above, Z_{eff} is the effective atomic number as screened by the closed electron shells; r_i is the distance of the ith electron to the point-charge nucleus; r_{ij} is the distance between two electrons; α is the fine-structure constant; V is the effective central potential in which the valence electrons move; $\boldsymbol{s}_i$ is the electron spin; and $\boldsymbol{l}_i$ is the electron angular momentum. Relativistic contributions may be derived from the Breit Hamiltonian resulting in two-body interactions including spin-spin ($\boldsymbol{s}_i \cdot \boldsymbol{s}_j$), spin-other-orbit ($\boldsymbol{s}_i \cdot \boldsymbol{l}_j$) [2,47–52], and orbit-orbit ($\boldsymbol{l}_i \cdot \boldsymbol{l}_j$) [2,49,52–54]. These interactions can be expressed as

$$\mathcal{H}_{\mathrm{s\text{-}s}} = \alpha^2 \sum_{i>j}\left[\frac{(\boldsymbol{s}_i \cdot \boldsymbol{s}_j)}{r_{ij}^3} - \frac{3(\boldsymbol{r}_{ij} \cdot \boldsymbol{s}_i)(\boldsymbol{r}_{ij} \cdot \boldsymbol{s}_j)}{r_{ij}^5}\right], \tag{A6}$$

$$\mathcal{H}_{\mathrm{o\text{-}o}} = -\frac{\alpha^2}{2}\sum_{i<j}\left[\frac{(\boldsymbol{p}_i \cdot \boldsymbol{p}_j)}{r_{ij}} + \frac{(\boldsymbol{r}_{ij} \cdot (\boldsymbol{r}_{ij} \cdot \boldsymbol{p}_i)\boldsymbol{p}_j)}{r_{ij}^3}\right], \tag{A7}$$

$$\mathcal{H}_{\mathrm{s\text{-}o\text{-}o}} = -\alpha^2 \sum_{i>j}\left(\frac{\boldsymbol{r}_{ij}}{r_{ij}^3} \times \boldsymbol{p}_i\right) \cdot (\boldsymbol{s}_i + 2\boldsymbol{s}_j), \tag{A8}$$

where $\boldsymbol{p}_i$ is the electron momentum. The action of the host is included as an effective potential with a symmetry appropriate for the crystal host. In its original inception [83], the crystal field was understood to have a purely electrostatic origin, such that a charge density $\rho(\boldsymbol{R})$ has an associated potential given by

$$V_{\mathrm{CF}}(\boldsymbol{r}_i) = \int \frac{\rho(\boldsymbol{R})}{|\boldsymbol{r}_i - \boldsymbol{R}|} d\boldsymbol{R}, \tag{A9}$$

and such that $\mathcal{H}_{\mathrm{CF}} = \sum_i (-e) V_{\mathrm{CF}}(\boldsymbol{r}_i)$. Presently, the electrostatic interpretation of the crystal field is not considered to be accurate [84]. However, the symmetry arguments that lead to its mathematical form as an expansion in spherical harmonics are still valid and are independent of the electrostatic interpretation. Table V summarizes the mapping from the Hamiltonian in Eq. (1) to the parametric Hamiltonian in Eq. (2).

APPENDIX B: ORTHOGONAL AND NON-ORTHOGONAL OPERATORS

In 1984, Judd, Crosswhite, and Suskin [20,41] discussed the usefulness of a complete set of orthogonal operators composing the parametric Hamiltonian. The purpose of orthogonal operators is to remove correlations between the parameters during the fitting procedure, so that in the case of parameters included sequentially, the new and less important parameter will make minimal changes to the previous ones. Consequently, the correlations when using non-orthogonal operators result in larger uncertainties in the parameters, as compared to the orthogonalized version [85]. Judd *et al.* derived the orthogonal operators related to the Coulomb interaction for both the single configuration $\hat{f}_k$ [with coefficients $F^{(k)}$] and the configuration interaction $\hat{e}_\alpha$, $\hat{e}_\beta$, $\hat{e}_\gamma$, and $\hat{t}_2$ [with coefficients, $\alpha, \beta, \gamma, T^{(2)}$, respectively]. In fact, the orthogonal operators for the single configuration description are better quantified in terms of the operators $\hat{e}_k^{\perp}$ [and coefficients $E_{\perp}^{(k)}$], as they obey simpler transformation properties with respect to $\hat{C}(\mathcal{G}_2)$ and $\hat{C}(\mathcal{SO}(7))$ used to classify the states [2]. On the other hand, the same energy spectrum, for both the orthogonal and non-orthogonal version of the parametric Hamiltonian, can be obtained if one realizes a mapping between the set of coefficients related to each one, as detailed below.

We notice that, although the argument for using orthogonal operators was already established five years earlier, Carnall *et al.* [21] decided to use the non-orthogonal operators in their calculations, as in Eq. (2). However, later reference tables for three-body operators from Hansen, Judd, and Crosswhite [39] provide matrix-element values for the orthogonalized operator $\langle\psi_i|\hat{t}_2^{\perp}|\psi_j\rangle$ [86], rather than for $\langle\psi_i|\hat{t}_2|\psi_j\rangle$. Any attempt of using the $T^{(2)}$ parameters from Ref. [21] as coefficient to the matrix elements in Ref. [39] will lead to wrong results.

We end by mentioning that the transformation below is not complete, because the operators corresponding to the $M^{(k)}$ and $P^{(k)}$ parameters are not orthogonal between themselves. This lingering part of the Hamiltonian may be orthogonalized using the $\hat{z}_i$ operators initially described by Judd, Crosswhite, and Crosswhite in their description of the intra-atomic magnetic interactions [40] and explained in Ref. [64]. However, we will not consider it here, because it adds additional parameters that have not seen wide adoption.

1. Relation between orthogonal and non-orthogonal Hamiltonians

We start by defining the Hamiltonians in both forms, orthogonal,

$$\mathcal{H}^{\mathrm{ortho}} = E'^{(0)}\hat{e}'_0 + E'^{(1)}\hat{e}'_1 + E'^{(3)}\hat{e}'_3 + \alpha'\hat{e}'_\alpha + \beta'\hat{e}'_\beta + \gamma'\hat{e}'_\gamma + T'^{(2)}\hat{t}'_2, \tag{B1}$$

(here, we use the $'$ symbol for representing the orthogonal operators and parameters) and non-orthogonal,

$$\mathcal{H}^{\mathrm{non}} = E^{(0)}\hat{e}_0 + E^{(1)}\hat{e}_1 + E^{(3)}\hat{e}_3 + \alpha\hat{e}_\alpha + \beta\hat{e}_\beta + \gamma\hat{e}_\gamma + T^{(2)}\hat{t}_2, \tag{B2}$$

in which we have only selected the elements that matter for current discussion, and not the full parametric Hamiltonian as written in Eq. (2) in the main text. Furthermore, Eq. (2) is written in terms of $\hat{f}_0$, $\hat{f}_2$, $\hat{f}_4$, $\hat{f}_6$ operators instead of $\hat{e}_0$, $\hat{e}_1$, $\hat{e}_3$; however, there is a straight forward relation between them that will be provided below. Finally, by comparison with Eq. (2), notice that

$$\hat{e}_\alpha = \hat{L}^2, \quad \hat{e}_\beta = \hat{C}(\mathcal{G}_2), \quad \hat{e}_\gamma = \hat{C}(\mathcal{S}O_7). \tag{B3}$$

TABLE V. A summary of the mapping from the Hamiltonian in Eq. (1) to the parametric Hamiltonian in Eq. (2).

Hamiltonian	Parametric Hamiltonian	Origin
$\mathcal{H}_K + \mathcal{H}_n$	$\mathcal{H}_0$	single configuration
$\mathcal{H}_{e\text{-}e}$	$F^{(k)}, \quad k = 0, 2, 4, 6$	single configuration
$\mathcal{H}_{e\text{-}e}$	α, β, γ + screening $F^{(k)}$	configuration interaction via $\langle\psi\|G\|m\rangle\langle m\|G\|\psi'\rangle/\Delta E_m$
$\mathcal{H}_{e\text{-}e}$	$T^{(k)}, \quad k = 3, 4, 6, 7, 8$	same as the above, for the cases that $\|\psi\rangle$ and $\|m\rangle$ differ in one electron
$\mathcal{H}_{e\text{-}e}$	$T^{(k)}, \quad k = 11, \ldots, 19$	configuration interaction, third order perturbation theory
$\mathcal{H}_{\text{s-o}}$	ζ	single configuration
$\mathcal{H}_{e\text{-}e} + \mathcal{H}_{\text{s-o}}$	$P^{(k)} + M^{(k)}$ + screening ζ	configuration interaction via $\langle\psi\|\Lambda\|m\rangle\langle m\|G\|\psi'\rangle/\Delta E_m$
$\mathcal{H}_{\text{s-s}}$	$M^{(k)}, \quad k = 0, 2, 4$	single configuration
$\mathcal{H}_{\text{s-o-o}}$	$M^{(k)}$ + screening ζ	single configuration
$\mathcal{H}_{\text{o-o}}$	α, β, γ	single configuration
$\mathcal{H}_{\text{CF}}$	$\mathcal{B}_q^{(k)}, \quad k = 2, 4, 6, \quad q = -k, \ldots, k$	single configuration

The relations between orthogonal and non-orthogonal operators are provided in Ref. [20], that we replicate here for convenience,

$$\hat{e}'_0 = \hat{e}_0, \tag{B4}$$

$$\hat{e}'_1 = \hat{e}_1 - \frac{9\hat{e}_0}{13}, \tag{B5}$$

$$\hat{e}'_3 = \hat{e}_3, \tag{B6}$$

$$\hat{e}'_\alpha = \frac{\hat{e}_3}{2} + \frac{5\hat{L}^2}{4} - 30\hat{C}(\mathcal{G}_2), \tag{B7}$$

$$\hat{e}'_\beta = 5\hat{C}(\mathcal{S}O_7) - 6\hat{C}(\mathcal{G}_2), \tag{B8}$$

$$\hat{e}'_\gamma = \frac{25\hat{C}(\mathcal{S}O_7)}{2} - \frac{15N}{2} + \frac{3\hat{e}_0}{2} - \frac{\hat{e}_1}{2}, \tag{B9}$$

$$\hat{t}'_2 = \hat{t}_2 - \frac{(N-2)\hat{e}_3}{70\sqrt{2}}, \tag{B10}$$

where N is the number of electrons in the f shell. Next, we replace those definitions into $\mathcal{H}^{\text{ortho}}$ and rearrange the terms to obtain

$$\begin{aligned}\mathcal{H}^{\text{ortho}} = &\left(E'^{(0)} - \frac{9E'^{(1)}}{13} + \frac{3\gamma'}{2}\right)\hat{e}_0 + \left(E'^{(1)} - \frac{\gamma'}{2}\right)\hat{e}_1 \\ &+ \left(E'^{(3)} + \frac{\alpha'}{2} - \frac{T'^{(2)}(N-2)}{70\sqrt{2}}\right)\hat{e}_3 \\ &+ \frac{5\alpha'}{4}\hat{L}^2 - (\beta' 6 + \alpha' 30)\hat{C}(\mathcal{G}_2) \\ &+ \left(\gamma'\frac{25}{2} + \beta' 5\right)\hat{C}(\mathcal{S}O_7) - \gamma'\frac{15N}{2} + T'^{(2)}\hat{t}_2.\end{aligned} \tag{B11}$$

Comparing the coefficients above with non-orthogonal Hamiltonian $\mathcal{H}^{\text{non}}$, acknowledging Eqs. (B3), both Hamiltonians become the same (disregarding the constant term) for the following relations:

$$E^{(0)} = E'^{(0)} - \frac{9E'^{(1)}}{13} + \frac{3\gamma'}{2}, \tag{B12}$$

$$E^{(1)} = E'^{(1)} - \frac{\gamma'}{2}, \tag{B13}$$

$$E^{(3)} = E'^{(3)} + \frac{\alpha'}{2} - \frac{(N-2)T'^{(2)}}{70\sqrt{2}}, \tag{B14}$$

$$\alpha = \frac{5\alpha'}{4}, \tag{B15}$$

$$\beta = -(6\beta' + 30\alpha'), \tag{B16}$$

$$\gamma = \frac{25}{2}\gamma' + 5\beta', \tag{B17}$$

$$T^{(2)} = T'^{(2)}. \tag{B18}$$

Inverting the identities above for α', β', γ', and $T'^{(2)}$ we find the following relations,

$$E'^{(1)} = E^{(1)} + \frac{4\alpha}{5} + \frac{\beta}{30} + \frac{\gamma}{25}, \tag{B19}$$

$$E'^{(2)} = E^{(2)}, \tag{B20}$$

$$E'^{(3)} = E^{(3)} - \frac{2\alpha}{5} + \frac{T^{(2)}(N-2)}{70\sqrt{2}}, \tag{B21}$$

$$\alpha' = \frac{4\alpha}{5}, \tag{B22}$$

$$\beta' = -4\alpha - \frac{\beta}{6}, \tag{B23}$$

$$\gamma' = \frac{8\alpha}{5} + \frac{\beta}{15} + \frac{2\gamma}{25}, \tag{B24}$$

$$T'^{(2)} = T^{(2)}. \tag{B25}$$

Now, we are left with the task of relating the $E^{(k)}$ parameters with the $F^{(k)}$ parameters used in Eq. (2). However, those are well explained in Chap. 2 Sec. 9 of Ref. [2], that kindly provides a direct relation between coefficients as the following:

$$E^{(1)} = \tfrac{1}{9}(70F_2 + 231F_4 + 2002F_6), \tag{B26}$$

$$E^{(2)} = \tfrac{1}{9}(F_2 - 3F_4 + 7F_6), \tag{B27}$$

$$E^{(3)} = \tfrac{1}{3}(5F_2 + 6F_4 - 91F_6), \tag{B28}$$

in which we used the subindex notation that relates to the superindex notation $F^{(k)} = D_k F_k$, as presented in Eq. (2), through the constant values $D_2 = 225$, $D_4 = 1089$, and $D_6 = 184041/25$; see Table 6-2 in Ref. [55].

We emphasize that the transformation above is not the complete story, because for a completely orthogonal parametric Hamiltonian, we would still need to orthogonalize the

TABLE VI. Fitted model parameters using `qlanth` with orthogonal operators. Parameters in square brackets were held fixed during fitting. In the case of Eu, Gd, and Tb, some $E_\perp^{(i)}$ parameters were constrained according to $E_\perp^{(2)} = 0.0049E_\perp^{(1)}$, and/or $E_\perp^{(3)} = 0.098E_\perp^{(1)}$. The parameters for Pm are interpolated. σ_{REF} and n_{REF} are from Carnall *et al.* [21]. The data was fitted in the following order: Pr, Nd, Dy, Ce, Sm, Ho, Er, Tm, Yb, Tb, Eu, Gd.

	Ce	Pr	Nd	Pm	Sm	Eu	Gd	Tb	Dy	Ho	Er	Tm	Yb
$E_\perp^1$		4611.2(0.8)	4904(2)	[5182]	5378.2(0.5)	5493(0.4)	5794.4(0.2)	6026(1)	6240(9)	6434(1)	6651(1)	6828(2)	
$E_\perp^2$		22.05(0.01)	23.68(0.02)	[25]	26.11(0.02)	[27]	[28]	[30]	30.84(0.03)	31.57(0.05)	33(0.01)	34.02(0.01)	
$E_\perp^3$		460.73(0.08)	487.94(0.09)	[514]	540.2(0.1)	[538]	583.7(0.1)	608.9(0.5)	631(1)	654(0.4)	680.34(0.09)	672.7(0.1)	
ζ	645.4(0.3)	749.8(0.8)	885(1)	[1023]	1175(1)	1342(0.4)	1498(1)	1706(1)	1911(1)	2144(1)	2377(1)	2633.7(0.5)	2914.6(0.4)
$\alpha_\perp$		12.91(0.08)	17.1(0.09)	[15]	16.13(0.07)	[15]	14.39(0.05)	14.36(0.06)	14.3(0.2)	14(0.1)	13.85(0.09)	13.6(0.1)	
$\beta_\perp$		28.3(0.9)	12.7(0.8)	[20]	14(1)	[23]	[24]	14(3)	32(1)	33(1)	28.4(0.7)	33(1)	
$\gamma_\perp$		97.7(0.3)	109(1)	[110]	[115]	[120]	[124]	[129]	133(4)	[138]	[143]	[148]	
$T_\perp^2$			291(5)	[294]	[296]	[299]	[301]	[303]	300(10)	[308]	[310]		
T^3			35(2)	[37]	[39]	[39]	[40]	[41]	46(6)	39(2)	44(2)		
T^4			59(2)	[69]	[72]	[77]	[81]	[85]	90(20)	118(7)	68(3)		
T^6			−287(5)	[−313]	−344(9)	[−302]	[−296]	−280(10)	−320(20)	−240(20)	−270(6)		
T^7			338(6)	[355]	364(8)	[349]	[345]	330(10)	390(10)	310(20)	300(10)		
T^8			305(8)	[332]	339(5)	[327]	[324]	385(8)	315(8)	290(10)	290(10)		
M^0		1.8(0.1)	2.1(0.1)	[2]	2.5(0.1)	[2]	2.9(0.1)	2.5(0.1)	3.1(0.1)	2.2(0.1)	3.9(0.1)	3.8(0.1)	
P^2		−30(20)	210(20)	[232]	330(30)	[342]	560(50)	450(40)	650(30)	530(30)	720(30)	630(20)	
B_0^2	[−237]	−221(7)	−250(10)	[−214]	−140(20)	−190(10)	[−226]	−240(20)	−230(10)	[−213]	−246(9)	−257(8)	[−249]
B_0^4	[645]	730(10)	500(60)	[531]	240(50)	440(20)	[498]	620(40)	570(50)	520(30)	350(50)	450(10)	[412]
B_0^6	[766]	670(20)	640(40)	[578]	590(50)	530(20)	[477]	260(30)	180(40)	410(30)	560(40)	310(20)	[305]
B_2^2	[−98]	−126(5)	−50(9)	[−90]	[−80]	[−91]	[−91]	−90(10)	−60(10)	−100(10)	−99(9)	−101(5)	[−94]
B_2^4	[518]	420(10)	500(30)	[470]	690(30)	[416]	[389]	260(20)	190(30)	250(20)	350(30)	300(10)	[244]
B_2^6	[−926]	−910(10)	−830(30)	[−812]	−690(30)	[−726]	[−682]	−730(20)	−660(20)	−560(20)	−410(30)	−450(10)	[−404]
B_4^4	[599]	600(10)	560(30)	[535]	380(30)	[511]	[498]	490(20)	550(20)	490(20)	390(30)	430(10)	[423]
B_4^6	[−429]	−350(10)	−400(20)	[−360]	−430(30)	[−314]	[−292]	−240(20)	−150(40)	−200(20)	−190(20)	−240(20)	[−160]
B_6^6	[−866]	−780(10)	−830(30)	[−750]	−750(40)	[−680]	[−645]	−510(30)	−550(30)	−550(20)	−510(20)	−500(10)	[−452]
ε	7	−2	−4		−14	−14	−7	−2	−8	−3	−7	−11	−11
n	7	75	146		233	29	70	146	198	204	127	56	5
σ	47	16	14		13	14	8	8	11	9	18	13	60
nRef	7	75	146		232	29	70	146	198	204	127	56	5
σRef	51	16	14		13	16	10	12	12	10	19	10	38

operators related to the M and P coefficients. This lingering part of the Hamiltonian may be made orthogonal using the $\hat{z}_i$ operators initially described by Judd, Crosswhite, and Crosswhite in their description of the intra-atomic magnetic interactions [40] and explained in Ref. [64]. However, we will not consider it here, as it adds additional parameters that are not yet well explored in the literature. Having said that, the full orthogonal Hamiltonian considered here is parametrized as

$$\begin{aligned}\mathcal{H}_{\mathrm{para}}^{\mathrm{ortho}} = (\mathcal{H}_0 + \epsilon) &\sum_{k=0,2,4,6} E'^{(k)}\hat{e}'_k + \zeta \sum_{i=1}^{N}(\hat{s}_i \cdot \hat{l}_i) \\ &+ \alpha'\hat{e}'_\alpha + \beta'\hat{e}'_\beta + \gamma'\hat{e}'_\gamma \\ &+ T'^{(2)}\hat{t}'_2 + \sum_{k=2,3,4,6,7,8} T^{(k)}\hat{t}_k \\ &+ \sum_{k=2,4,6} P^{(k)}\hat{p}_k + \sum_{k=0,2,4} M^{(k)}\hat{m}_k \\ &+ \sum_{i=1}^{N}\sum_{k=2,4,6}\sum_{q=-k}^{k} \mathcal{B}_q^{(k)}\hat{C}_q^{(k)}(i). \end{aligned} \tag{B29}$$

Table VI shows the fitted parameters in $\mathcal{H}_{\mathrm{para}}^{\mathrm{ortho}}$; notice the equivalence in notations $(') \equiv (\perp)$. The fitting procedure used the same sequential manner as described in the main paper, i.e., building up regression models for the parameters that are held fixed while fitting. Contrasting the orthogonal and non-orthogonal approaches against Carnall *et al.* [21], Table III in the main text shows σ to be smaller than those values quoted by Carnall *et al.* in 2 out of 12 cases. For the approach with the orthogonal operator basis shown here, in Table VI we found σ to be smaller in 7 out of 12 cases. That shows the expected tendency of the orthogonal approach leading to better fittings.

Note that the parameters for Ce, Pr, Nd, and Dy in Tables III and VI seem to coincide, including the orthogonalized parameters, as they are related by Eqs. (B19)–(B28) in the main text. That reflects the deterministic approach taken here and described in the main text. The fitting initial conditions are the same in both approaches, leading to similar converged values, although not exactly equal within the numerical precision. This fact changes for Sm (the next element in the fitting), because a regression made for fixing γ (non-orthogonal) and $\gamma_\perp$ (orthogonal) lead to different results. The same is true for the subsequent fittings. Finally, we also compared the relative uncertainties in both tables, and unexpectedly, we found that the orthogonal basis leads to larger uncertainty values on average (9 out of 12 cases).

APPENDIX C: GLOBAL FITTING ANALYSIS

In the main text, we employed the same Levenberg-Marquardt method used in Ref. [21] to obtain the fitted parameters. In order to test whether or not we have found a global minimum, we decided to try a stochastic optimization algorithm. In particular, we used the method Adam [87] from the PyTorch library [88]. Note that `qlanth` has the feature of exporting the Hamiltonian to Python. We exemplify the point by finding new parameters for Er^{3+}:LaF_3. We always used the values in Ref. [21] as initial guess, among the many attempts performed. We avoided exploring parameter values too far from the original guess, because we know it has physical significance and serves as a meaningful reference point. This is controlled by the learning rate (lr) parameter that we typically set $lr = 0.1$. We checked that 2000 iterations usually led to a good convergence, although we made attempts up to 50 000 iterations. Our code is available at Ref. [89]. As a result, we could bring the average agreement to the experimental energy levels (σ, as described in the main text) down to $\sigma = 15\ \mathrm{cm}^{-1}$, which is a 20% improvement over the value quoted in Ref. [21]. The set of new parameters are listed in Table VII.

TABLE VII. Fitted parameters for Er^{3+}:LaF_3 using the Adam method from PyTorch Library. Values with their uncertainties given in cm^{-1}. Values for γ and $T^{(2)}$ were held fixed during fitting.

Parameter	Value	Parameter	Value
$F^{(2)}$	97 592(71)	$T^{(6)}$	−289(23)
$F^{(4)}$	68 036(142)	$T^{(7)}$	336(38)
$F^{(6)}$	54 187(136)	$T^{(8)}$	364(39)
ζ	2377(5)	$B_0^{(2)}$	−242(33)
α	17.3(0.5)	$B_0^{(4)}$	367(238)
β	−583(21)	$B_0^{(6)}$	522(191)
γ	[1800]	$B_2^{(2)}$	−96(29)
$M^{(0)}$	3.8(0.4)	$B_2^{(4)}$	357(126)
$P^{(2)}$	700(141)	$B_2^{(6)}$	−424(142)
$T^{(2)}$	[400]	$B_4^{(4)}$	417(115)
$T^{(3)}$	45(10)	$B_4^{(6)}$	−203(85)
$T^{(4)}$	67(12)	$B_6^{(6)}$	−513(111)

[1] J. H. V. Vleck, The puzzle of rare-earth spectra in solids, J. Phys. Chem. **41**, 67 (1937).

[2] B. Wybourne, *Spectroscopic Properties of Rare Earths* (Interscience Publishers, New York, 1965).

[3] G. Liu and B. Jacquier, *Spectroscopic Properties of Rare Earths in Optical Materials*, Springer Series in Materials Science (Springer, New York, 2005).

[4] L. D. DeLoach, S. A. Payne, L. Chase, L. K. Smith, W. L. Kway, and W. F. Krupke, Evaluation of absorption and emission properties of Yb^{3+} doped crystals for laser applications, IEEE J. Quantum Electron. **29**, 1179 (1993).

[5] C. Jørgensen and R. Reisfeld, *Lasers and Excited States of Rare Earths* (Springer, Berlin, 1977).

[6] Z. Wei, Y. Liu, B. Li, J. Li, S. Lu, X. Xing, K. Liu, F. Wang, and H. Zhang, Rare-earth based materials: An effective toolbox for brain imaging, therapy, monitoring and neuromodulation, Light Sci. Appl. **11**, 175 (2022).

[7] M. Atatüre, D. Englund, N. Vamivakas, S.-Y. Lee, and J. Wrachtrup, Material platforms for spin-based photonic quantum technologies, Nat. Rev. Mater. **3**, 38 (2018).

[8] D. D. Awschalom, R. Hanson, J. Wrachtrup, and B. B. Zhou, Quantum technologies with optically interfaced solid-state spins, Nat. Photonics **12**, 516 (2018).

[9] P. Stevenson, C. M. Phenicie, I. Gray, S. P. Horvath, S. Welinski, A. M. Ferrenti, A. Ferrier, P. Goldner, S. Das, R. Ramesh, R. J. Cava, N. P. de Leon, and J. D. Thompson, Erbium-implanted materials for quantum communication applications, Phys. Rev. B **105**, 224106 (2022).

[10] M. T. Uysal, Ł. Dusanowski, H. Xu, S. P. Horvath, S. Ourari, R. J. Cava, N. P. de Leon, and J. D. Thompson, Spin-photon entanglement of a single Er^{3+} ion in the telecom band, Phys. Rev. X **15**, 011071 (2025).

[11] Z. Rudzikas, *Theoretical Atomic Spectroscopy* (Cambridge University Press, Cambridge, 2007).

[12] T. H. Taminiau, S. Karaveli, N. F. van Hulst, and R. Zia, Quantifying the magnetic nature of light emission, Nat. Commun. **3**, 979 (2012).

[13] D. Li, S. Karaveli, S. Cueff, W. Li, and R. Zia, Probing the combined electromagnetic local density of optical states with quantum emitters supporting strong electric and magnetic transitions, Phys. Rev. Lett. **121**, 227403 (2018).

[14] S. P. Horvath, C. M. Phenicie, S. Ourari, M. T. Uysal, S. Chen, t. Dusanowski, M. Raha, P. Stevenson, A. T. Turflinger, R. J. Cava, N. P. de Leon, and J. D. Thompson, Strong purcell enhancement of an optical magnetic dipole transition, arXiv:2307.03022.

[15] C. M. Dodson and R. Zia, Magnetic dipole and electric quadrupole transitions in the trivalent lanthanide series: Calculated emission rates and oscillator strengths, Phys. Rev. B **86**, 125102 (2012).

[16] G. Ofelt, Intensities of crystal spectra of rare-earth ions, J. Chem. Phys. **37**, 511 (1962).

[17] M. P. Hehlen, M. G. Brik, and K. W. Kramer, 50th anniversary of the Judd–Ofelt theory: An experimentalist's view of the formalism and its application, J. Lumin. **136**, 221 (2013).

[18] J.-P. R. Wells, S. P. Horvath, and M. F. Reid, Temperature dependent infrared absorption, crystal-field and intensity analysis of Ce^{3+} doped $LiYF_4$, Opt. Mater. **47**, 30 (2015).

[19] S. Ourari, Ł. Dusanowski, S. P. Horvath, M. T. Uysal, C. M. Phenicie, P. Stevenson, M. Raha, S. Chen, R. J. Cava, N. P. de Leon, and J. D. Thompson, Indistinguishable telecom band photons from a single Er ion in the solid state, Nature (London) **620**, 977 (2023).

[20] B. R. Judd and H. Crosswhite, Orthogonalized operators for the f shell, J. Opt. Soc. Am. B **1**, 255 (1984).

[21] W. T. Carnall, G. L. Goodman, K. Rajnak, and R. S. Rana, A systematic analysis of the spectra of the lanthanides doped into single crystal LaF_3, J. Chem. Phys. **90**, 3443 (1989).

[22] P. Novák, J. Kuneš, and K. Knížek, Crystal field of rare-earth impurities in LaF_3, Opt. Mater. **37**, 414 (2014).

[23] K. Binnemans, Interpretation of europium(III) spectra, Coord. Chem. Rev. **295**, 1 (2015).

[24] J. Cheng, W. Jun, C. Yonghu, Y. Min, and D. Changkui, Crystal-field analyses for trivalent lanthanide ions in $LiYF_4$, J. Rare Earths **34**, 1048 (2016).

[25] C. Görller-Walrand and K. Binnemans, Rationalization of crystal-field parametrization, Handbook Phys. Chemistry Rare Earths **23**, 121 (1996).

[26] L. Soderholm, C.-K. Loong, G. L. Goodman, and B. D. Dabrowski, Crystal-field splittings and magnetic properties of Pr^{3+} and Nd^{3+} in $RBa_2Cu_3O_7$, Phys. Rev. B **43**, 7923 (1991).

[27] C.-K. Loong, L. Soderholm, G. L. Goodman, M. M. Abraham, and L. A. Boatner, Ground-state wave functions of Tb^{3+} ions in paramagnetic $TbPO_4$: A neutron scattering study, Phys. Rev. B **48**, 6124 (1993).

[28] C. L. Li and M. F. Reid, Correlation-crystal-field analysis of the $^2H(2)_{11/2}$ multiplet of Nd^{3+}, Phys. Rev. B **42**, 1903 (1990).

[29] J. B. Gruber, J. R. Quagliano, M. F. Reid, F. S. Richardson, M. E. Hills, M. D. Seltzer, S. B. Stevens, C. A. Morrison, and T. H. Allik, Energy levels and correlation crystal-field effects in Er^{3+} doped garnets, Phys. Rev. B **48**, 15561 (1993).

[30] S. Mothkuri, M. F. Reid, J.-P. R. Wells, E. Lafitte-Houssat, P. Goldner, and A. Ferrier, Electron-nuclear interactions as a test of crystal field parameters for low-symmetry systems: Zeeman hyperfine spectroscopy of Ho^{3+}-doped Y_2SiO_5, Phys. Rev. B **103**, 104109 (2021).

[31] J. B. Gruber, M. E. Hills, T. H. Allik, C. K. Jayasankar, J. R. Quagliano, and F. S. Richardson, Comparative analysis of $Nd^{3+}(4f^3)$ energy levels in four garnet hosts, Phys. Rev. B **41**, 7999 (1990).

[32] K. Boldyrev, N. Kuz'min, A. Mukhin, V. Y. Ivanov, E. Dobretsova, E. Popova, S. Y. Gavrilkin, N. Leonyuk, V. Maltsev, B. Malkin, and M. N. Popova, Thermal and magnetic properties and optical spectroscopy of $SmCr_3(BO_3)_4$, Phys. Rev. Mater. **5**, 104413 (2021).

[33] X. Chen, G. Liu, J. Margerie, and M. F. Reid, A few mistakes in widely used data files for f^n configurations calculations, J. Lumin. **128**, 421 (2008).

[34] B. R. Judd and E. Lo, Three-electron matrix elements near the middle of the atomic f shell, J. Phys.: Condens. Matter **6**, L799 (1994).

[35] G. Racah, Theory of complex spectra. I, Phys. Rev. **61**, 186 (1942).

[36] G. Racah, Theory of complex spectra. II, Phys. Rev. **62**, 438 (1942).

[37] G. Racah, Theory of complex spectra. III, Phys. Rev. **63**, 367 (1943).

[38] G. Racah, Theory of complex spectra. IV, Phys. Rev. **76**, 1352 (1949).

[39] J. Hansen, B. Judd, and H. Crosswhite, Matrix elements of scalar three-electron operators for the atomic f shell, At. Data Nucl. Data Tables **62**, 1 (1996).

[40] B. Judd, H. Crosswhite, and H. Crosswhite, Intra-atomic magnetic interactions for f electrons, Phys. Rev. **169**, 130 (1968).

[41] B. Judd and M. Suskin, Complete set of orthogonal scalar operators for the configuration f^3, J. Opt. Soc. Am. B **1**, 261 (1984).

[42] B. Z. Malkin, R. V. Yusupov, I. F. Gilmutdinov, R. G. Batulin, A. G. Kiiamov, B. F. Gabbasov, S. I. Nikitin, and B. Barbara, Double-loop hysteresis of multisite dilute $Sr(Y_{1-x}Dy_x)_2O_4$ single crystal Kramers paramagnets: Electron-phonon interaction, quantum tunneling, and cross relaxation, Phys. Rev. B **109**, 054434 (2024).

[43] N. Qureshi, B. Z. Malkin, S. X. M. Riberolles, C. Ritter, B. Ouladdiaf, G. Balakrishnan, M. Ciomaga Hatnean, and O. A. Petrenko, Magnetic structures of geometrically frustrated $SrGd_2O_4$ derived from powder and single-crystal neutron diffraction, Phys. Rev. B **105**, 014425 (2022).

[44] M. A. Hughes, N. A. Panjwani, M. Urdampilleta, N. Theodoropoulou, I. Wisby, K. P. Homewood, B. Murdin, T. Lindström, and J. D. Carey, Coupling of erbium-implanted silicon to a superconducting resonator, Phys. Rev. Appl. **16**, 034006 (2021).

[45] M. Baker, 1,500 scientists lift the lid on reproducibility, Nature (London) **533**, 452 (2016).

[46] J. Lizarazo Ferro, Qlanth: A Hamiltonian for the lanthanides, San Francisco (CA): GitHub (2024), https://github.com/zia-lab/qlanth, accessed: Jan 2025.

[47] H. Bethe and E. Salpeter, *Quantum Mechanics of One- and Two-Electron Atoms* (Springer, New York, 1957).

[48] M. Blume and R. E. Watson, Theory of spin-orbit coupling in atoms I. Derivation of the spin-orbit coupling constant, Proc. R. Soc. London A **270**, 127 (1962).

[49] B. G. Wybourne, *Symmetry Principles and Atomic Spectroscopy* (Wiley-Interscience, New York, 1970).

[50] M. Jones, Mutual spin-orbit and spin-spin interactions in atomic structure calculations, J. Phys. B **4**, 1422 (1971).

[51] B. Bransden and C. Joachain, *Physics of Atoms and Molecules*, Pearson Education (Prentice Hall, London, 2003).

[52] G. Drake, *Springer Handbook of Atomic, Molecular, and Optical Physics*, Springer Handbook of Atomic, Molecular, and Optical Physics, Vol. 1 (Springer, New York, 2006).

[53] A. Abragam and J. H. Van Vleck, Theory of the microwave Zeeman effect in atomic oxygen, Phys. Rev. **92**, 1448 (1953).

[54] S. Yanagawa, Orbit-orbit interactions in atomic l^n configurations, J. Phys. Soc. Jpn. **10**, 1029 (1955).

[55] R. Cowan, *The Theory of Atomic Structure and Spectra*, Los Alamos Series in Basic and Applied Sciences (University of California Press, Los Angeles, 1981).

[56] G. H. Dieke, H. M. Crosswhite, and B. Dunn, Emission spectra of the doubly and triply ionized rare earths, J. Opt. Soc. Am. **51**, 820 (1961).

[57] K. Rajnak and B. G. Wybourne, Configuration interaction effects in l^N configurations, Phys. Rev. **132**, 280 (1963).

[58] B. R. Judd, Three-particle operators for equivalent electrons, Phys. Rev. **141**, 4 (1966).

[59] L. van Pieterson, M. F. Reid, G. W. Burdick, and A. Meijerink, $4f^n \rightarrow 4f^{(n-1)}5d$ Transitions of the heavy lanthanides: Experiment and theory, Phys. Rev. B **65**, 045114 (2002).

[60] P. S. Peijzel, P. Vergeer, A. Meijerink, M. F. Reid, L. A. Boatner, and G. W. Burdick, $4f^{(n-1)}5d \rightarrow 4f^n$ Emission of Ce^{3+}, Pr^{3+}, Nd^{3+}, Er^{3+}, and Tm^{3+} in $LiYF_4$ and YPO_4, Phys. Rev. B **71**, 045116 (2005).

[61] K. Rajnak and B. G. Wybourne, Electrostatically correlated spin-orbit interactions in l^N-type configurations, Phys. Rev. **134**, A596 (1964).

[62] H. H. Marvin, Mutual magnetic interactions of electrons, Phys. Rev. **71**, 102 (1947).

[63] Y. Y. Yeung and P. A. Tanner, New analyses of energy level datasets for $LaCl_3$: Ln^{3+} (Ln = Pr, Nd, Er), J. Alloys Compd. **575**, 54 (2013).

[64] J.-F. Wyart, A. Meftah, J. Sinzelle, W.-U. L. Tchang-Brillet, N. Spector, and B. R. Judd, Theoretical study of ground-state configurations $4f^n$ in Nd IV, Pr IV and Nd V, J. Phys. B **41**, 085001 (2008).

[65] V. Zhorin, Spectra (2015), https://github.com/vzhorin/Spectra, accessed: Oct 2024.

[66] M. Reid, Linuxemp (2018), http://www2.phys.canterbury.ac.nz/~mfr24/emp/, accessed: Sep 2024.

[67] See Supplemental Material at http://link.aps.org/supplemental/10.1103/llzb-wrlg for corrections to the *fncross* tables, documents typographical errors in previously reported energy levels, additional details regarding truncation, the parameter table for the trivalent lanthanide ions in $LiYF_4$, and a description of the electronic files, which includes Ref. [90].

[68] S. Edvardsson and D. Åberg, An atomic program for energy levels of equivalent electrons: Lanthanides and actinides, Comput. Phys. Commun. **133**, 396 (2001).

[69] S. Horvath, Pycf (2021), https://bitbucket.org/sebastianhorvath/pycf/src/master/, accessed: Aug 2025.

[70] J. Longdell, Dieke (2018), https://github.com/jevonlongdell/dieke, accessed: Aug 2025.

[71] L. Fiorucci, NJA-CFS (not just another crystal field software) (2025), https://github.com/letiziafiorucci/NJA-CFS, accessed: Aug 2025.

[72] L. Fiorucci and E. Ravera, Not just another crystal field software, J. Comput. Chem. **46**, e70063 (2025).

[73] D. I. Khomskii, Review—Orbital physics: Glorious past, bright future, ECS J. Solid State Sci. Technol. **11**, 054004 (2022).

[74] K. Levenberg, A method for the solution of certain non-linear problems in least squares, Q. Appl. Math. **2**, 164 (1944).

[75] D. W. Marquardt, An algorithm for least-squares estimation of nonlinear parameters, J. Soc. Ind. Appl. Math. **11**, 431 (1963).

[76] P. R. Bevington and D. K. Robinson, *Data Reduction and Error Analysis* (McGraw Hill, New York, 2003), Chap. 11.

[77] `qlanth` also implements calculations of forced electric dipole transitions.

[78] G. A. Kumar, R. Riman, E. Snitzer, and J. Ballato, Solution synthesis and spectroscopic characterization of high Er^{3+} content LaF_3 for broadband 1.5 μm amplification, J. Appl. Phys. **95**, 40 (2004).

[79] D. Velkov, Multi-electron coefficients of fractional parentage for the p, d, and f shells, Ph.D. thesis, John Hopkins University, 2000.

[80] P. Siyushev, K. Xia, R. Reuter, M. Jamali, N. Zhao, N. Yang, C. Duan, N. Kukharchyk, A. D. Wieck, R. Kolesov, and J. Wrachtrup, Coherent properties of single rare-earth spin qubits, Nat. Commun. **5**, 3895 (2014).

[81] M. Zhong, M. P. Hedges, R. L. Ahlefeldt, J. G. Bartholomew, S. E. Beavan, S. M. Wittig, J. J. Longdell, and M. J. Sellars, Optically addressable nuclear spins in a solid with a six-hour coherence time, Nature (London) **517**, 177 (2015).

[82] N. L. Jobbitt, J.-P. R. Wells, M. F. Reid, S. P. Horvath, P. Goldner, and A. Ferrier, Prediction of optical polarization and high-field hyperfine structure via a parametrized crystal-field model for low-symmetry centers in Er^{3+}-doped Y_2SiO_5, Phys. Rev. B **104**, 155121 (2021).

[83] H. Bethe, Termaufspaltung in kristallen, Ann. Phys. **395**, 133 (1929).

[84] D. J. Newman and B. Ng, *Crystal Field Handbook* (Cambridge University Press, Cambridge, 2000), Vol. 2007.

[85] D. Newman, Operator orthogonality and parameter uncertainty, Phys. Lett. A **92**, 167 (1982).

[86] `qlanth` includes the flexibility to use either orthogonal or non-orthogonal operators.

[87] D. P. Kingma and J. Ba, Adam: A method for stochastic optimization, arXiv:1412.6980.

[88] A. Paszke, S. Gross, F. Massa, A. Lerer, J. Bradbury, G. Chanan, T. Killeen, Z. Lin, N. Gimelshein, L. Antiga, *et al.*, Pytorch: An imperative style, high-performance deep learning library, *Proceedings of the 33rd International Conference on Neural Information Processing Systems* (Curran Associates Inc., New York, 2019), pp. 8026–8037.

[89] T. O. Puel, Lanthanide fitting (2025), https://github.com/Tharnier/Lanthanide-Fitting/releases/tag/v1.0, accessed: Apr 2025.

[90] A. Beckert, M. Grimm, N. Wili, R. Tschaggelar, G. Jeschke, G. Matmon, S. Gerber, M. Müller, and G. Aeppli, Emergence of highly coherent two-level systems in a noisy and dense quantum network, Nat. Phys. **20**, 472 (2024).